

# Solving the Robot-World Hand-Eye(s) Calibration Problem with Iterative Methods

Amy Tabb · Khalil M. Ahmad Yousef

Received: 28 July 2016 / Accepted: 1 April 2017

**Abstract** Robot-world, hand-eye calibration is the problem of determining the transformation between the robot end-effector and a camera, as well as the transformation between the robot base and the world coordinate system. This relationship has been modeled as  $\mathbf{AX} = \mathbf{ZB}$ , where  $\mathbf{X}$  and  $\mathbf{Z}$  are unknown homogeneous transformation matrices. The successful execution of many robot manipulation tasks depends on determining these matrices accurately, and we are particularly interested in the use of calibration for use in vision tasks. In this work, we describe a collection of methods consisting of two cost function classes, three different parameterizations of rotation components, and separable versus simultaneous formulations. We explore the behavior of this collection

Amy Tabb

United States Department of Agriculture  
Agricultural Research Service  
Appalachian Fruit Research Laboratory  
Kearneysville, West Virginia, 25430, USA.  
E-mail: amy.tabb@usda.gov

Mention of trade names or commercial products in this publication is solely for the purpose of providing specific information and does not imply recommendation or endorsement by the U.S. Department of Agriculture. USDA is an equal opportunity provider and employer.

A. Tabb acknowledges the support of United States National Science Foundation grant number IOS-1339211.

Khalil M. Ahmad Yousef  
Computer Engineering Department  
The Hashemite University  
Zarqa 13115, Jordan.  
E-mail: khalil@hu.edu.jo

The citation information for this paper is:

A. Tabb and K. M. Ahmad Yousef, "Solving the robot-world hand-eye(s) calibration problem with iterative methods," *Machine Vision and Applications*, vol. 28, no. 5, pp. 569–590, Aug. 2017. doi: 10.1007/s00138-017-0841-7

We include an Erratum to this version of the paper. Please see Section 7 for details.

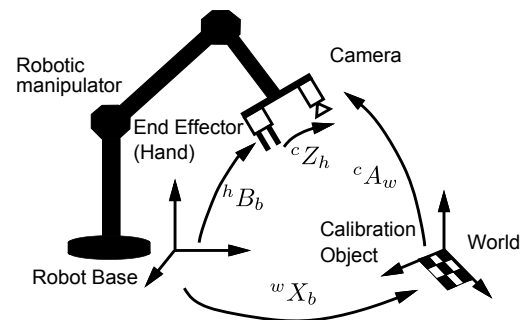


**Fig. 1** Hand-Eye Robot-World Calibration: A camera (eye) mounted at the end-effector (hand) of a robot.

of methods on real datasets and simulated datasets, and compare to seven other state-of-the-art methods. Our collection of methods return greater accuracy on many metrics as compared to the state-of-the-art. The collection of methods is extended to the problem of robot-world hand-multiple-eye calibration, and results are shown with two and three cameras mounted on the same robot.

## 1 Introduction

The robot-world hand-eye calibration problem consists of determining the homogeneous transformation matrices (HTMs) between the robot hand, or end-effector, to the camera, as well as the transformation of the robot base to the world coordinate system.

The preliminaries of the robot-world hand-eye calibration problem are as follows. Let the transformation from the hand coordinate frame to the camera coordinate frame be  ${}^c Z_h$  or simply  $\mathbf{Z}$ , and the transformation from the robot-base coordinate frame to the world coordinate frame be  ${}^w X_b$  or simply  $\mathbf{X}$ . The transformation

of the robot base frame to the hand coordinate frame is  ${}^h B_b$  or simply  $\mathbf{B}$ , and is assumed to be known from the robot controller. Finally, the transformation from the world coordinate frame to the camera coordinate frame is represented by HTM  ${}^c A_w$  or  $\mathbf{A}$ .  $\mathbf{A}$  is calculated using a camera calibration procedure such as Zhang [17], where the world coordinate frame is defined by a calibration object in the workspace. The transformations are illustrated by Figure 1. We note here that the labeling of the transformations in our version of the problem is different than that used in the traditional robot-world hand-eye calibration problem [18] in that some matrices are inverted ( $\mathbf{A}$ ,  $\mathbf{B}$ ) and the rest of matrices are exchanged ( $\mathbf{X}$ ,  $\mathbf{Z}$ ). Despite this difference, the linear relationship  $\mathbf{AX} = \mathbf{ZB}$  is still the same in our interpretation of the problem versus others. We interpreted the problem differently because by doing so we are able to simplify the derivation of some of the cost functions that we use in Section 2.2.

Given these preliminaries, Zhuang *et al.* [18] formalized the robot-world hand-eye calibration explicitly as the homogeneous matrix equation  $\mathbf{AX} = \mathbf{ZB}$ , where all of the matrices are  $4 \times 4$  matrices, and were the first to provide a method to find solutions for  $\mathbf{X}$  and  $\mathbf{Z}$ . Many different positions of the robot and camera are used to generate multiple relationships  $\mathbf{A}_i \mathbf{X} = \mathbf{ZB}_i$ ,  $i \in [0, n-1]$ , where  $n$  is the number of robot poses used for the calibration.

The robot-world hand-eye calibration problem is different, though related, to the hand-eye calibration problem, which was formulated as  $\mathbf{AX} = \mathbf{XB}$  by Shiu and Ahmad [11]. In the hand-eye calibration problem, the matrices  $\mathbf{A}_i$  and  $\mathbf{B}_i$  are now considered as the relative transformations from one pose to another. Use of relative transformations is problematic as decisions must be made as to how to convert absolute transformations into relative ones. This work considers instead  $\mathbf{A}_i$  and  $\mathbf{B}_i$  as poses with respect to the world coordinate system and robot base coordinate system, respectively, and as a result robot-world hand-eye calibration is needed.

We structure the paper as follows. In the rest of Section 1 and specifically in Subsection 1.1, we provide an overview of existing approaches and recent work. In Subsection 1.2, we discuss our approach and contributions to the robot-world hand-eye calibration problem. Section 2 introduces two classes of proposed methods and extends those classes to the multiple camera case. Section 3 describes the experiments, metrics, and implementation details. In Section 5, the results on real and simulated datasets are shown and discussed. Finally, in Section 6, we present our conclusions.

## 1.1 Recent work

Most recent work on the robot-world hand-eye calibration problem makes use of the decomposition of  $\mathbf{AX} = \mathbf{ZB}$  into a purely rotational part and a translational part, where  $\mathbf{R}_A$  represents a  $3 \times 3$  rotation matrix, and  $\mathbf{t}_A$  a  $3 \times 1$  translation vector as shown in Equation 1.

$$\begin{bmatrix} \mathbf{R}_A & \mathbf{t}_A \\ \mathbf{0}^T & 1 \end{bmatrix} \begin{bmatrix} \mathbf{R}_X & \mathbf{t}_X \\ \mathbf{0}^T & 1 \end{bmatrix} = \begin{bmatrix} \mathbf{R}_Z & \mathbf{t}_Z \\ \mathbf{0}^T & 1 \end{bmatrix} \begin{bmatrix} \mathbf{R}_B & \mathbf{t}_B \\ \mathbf{0}^T & 1 \end{bmatrix} \quad (1)$$

Methods utilizing the decomposition of the problem that is shown in Equation 1 into two parts are called separable methods. Separable methods cause Equation 1 to produce two other equations: the rotation part as represented by Equation 2 and the translation part as represented by Equation 3.

$$\mathbf{R}_A \mathbf{R}_X = \mathbf{R}_Z \mathbf{R}_B \quad (2)$$

$$\mathbf{R}_A \mathbf{t}_X + \mathbf{t}_A = \mathbf{R}_Z \mathbf{t}_B + \mathbf{t}_Z \quad (3)$$

Since Equation 3 is linear in  $\mathbf{t}_X$  and  $\mathbf{t}_Z$  if  $\mathbf{R}_Z$  is known, the most frequent approach to estimate  $\mathbf{X}$  and  $\mathbf{Z}$  is to first find  $\mathbf{R}_X$  and  $\mathbf{R}_Z$  using Equation 2, and then use that solution and Equation 3 to find  $\mathbf{t}_X$  and  $\mathbf{t}_Z$ .

Of those methods that separate the estimation of the rotation and translation parts using Equation 1, there are several different approaches. In Zhuang *et al.* [18], a linear solution was proposed for finding the unknowns  $\mathbf{R}_X$  and  $\mathbf{R}_Z$  by representing the rotation matrices as quaternions, and the translation components were found using linear least squares. Dornaika and Horaud in [3] gave a closed-form method for estimating the rotation components using quaternions, which did not require normalization like in [18]. Translation components were estimated with linear least squares as in [18]. Hirsh *et al.* in [4] proposed a separable, iterative approach in which the estimation of  $\mathbf{X}$  and  $\mathbf{Z}$  is alternated. The method consists of assuming that  $\mathbf{Z}$  is known and estimating  $\mathbf{X}$  by averaging  $\mathbf{X}_i = \mathbf{ZB}_i \mathbf{A}^{-1}$  for all  $i$  to generate an estimate for  $\mathbf{X}$ ; this process is repeated in a similar way for  $\mathbf{Z}$  using the estimate found for  $\mathbf{X}$ , and the estimation of  $\mathbf{X}$  and  $\mathbf{Z}$  is continued until termination conditions are met. Like the other methods in this group, estimation of rotation is separated from translation, and rotation is represented by quaternions. In the method of Shah [10], the Kronecker product and singular value decomposition were used to create a closed-form solution.

The second class of methods are typically called simultaneous solutions; they do not decouple rotation and translation error and thus have the advantage that error from the rotation estimation is not propagated to the translation estimation. In [3], in addition to a

closed-form separable solution, Dornaika and Horaud present a formulation of the problem as a non-linear least squares problem. The rotation components are represented by matrices, so there are 18 parameters for rotation and 6 for translation. The cost function contains penalty terms that enforce orthonormality of the rotation matrices. Following Dornaika and Horaud, Stobl and Hirzinger in [12] estimate the translation and rotation components through non-linear estimation techniques, though in their approach weights for the rotational and translational parts are chosen automatically and a position/orientation precision ratio parameter is required. The work of Li *et al.* [6] proposed a simultaneous solution that is found using dual quaternions and the Kronecker product.

Besides those approaches that deal with the equality  $\mathbf{AX} = \mathbf{ZB}$  in separable and simultaneous versions, there have been some approaches within the context of the hand-eye calibration problem to refine the estimation of the camera calibration parameters. For example, in [5], Horaud and Dornaika incorporated camera calibration parameters into a cost function for the hand-eye calibration problem  $\mathbf{AX} = \mathbf{XB}$  and solved using the Levenberg-Marquardt method when the rotations are represented by quaternions. In this method, the requirement that the quaternion must have unit norm was enforced using penalty terms. Recently, Malti [8] in a work about hand-eye calibration, incorporated a variation of the robot-world hand-eye calibration formulation and used reprojection error together with epipolar constraints to simultaneously refine the camera intrinsic and distortion parameters in addition to the  $\mathbf{X}$  and  $\mathbf{Z}$  HTMs. Unlike Horaud and Dornaika [5], Malti in [8] uses Euler angles to represent rotation and as a result his method does not need penalty terms.

## 1.2 Our approach and contributions

Our work on the robot-world hand-eye calibration problem is motivated by three particular situations. The first is that we use a robot-mounted camera for multi-view high-quality reconstruction of complicated objects such as leafless trees as in Tabb [13]; while some extrinsic camera calibration errors can be tolerated, the reconstruction outcomes improve when the camera calibration error is low. The second situation is where we use the same robot-mounted camera in laboratory or field conditions, where it can be the case that non-experts will be involved with performing calibration and acquiring data from a remote location. For this particular situation, our goal was to devise methods for robot-world hand-eye calibration that are not sensitive to the particular sequence of motions used during the calibration and is robust to

non-ideal calibration situations. Finally third, we have some situations in which multiple cameras are mounted on the same robot end-effector. While it is possible to only calibrate one camera using robot-world hand-eye calibration and then perform stereo camera calibration, we instead desired a way to calibrate all components at the same time so that error from one step is not propagated to the final calibration. This approach also allows cameras to have vastly different fields of view and does not require overlapping fields of view for any two cameras, which is more flexible than stereo calibration.

We note here that the robot-world hand-eye calibration problem has been discussed in the literature for more than two decades. Early contributions focused on linear and/or closed-form solutions because of computational efficiency. However, with the advent of open source nonlinear least square solvers, such as *levmar* [7] and Ceres [2], in addition to the general interest in bundle adjustment [16], iterative methods with previously unconsidered parameterizations of the rotational components offer advantages over the linear and closed-form approaches.

In this paper, we propose a collection of iterative methods for the robot-world hand-eye calibration problem. There are two classes of cost functions in this collection. The first class of cost functions minimizes the sum of squared difference between  $\mathbf{AX}$  and  $\mathbf{ZB}$  over  $n$  positions of the robot as given in Equation 4 below, or in a closely-related version of it, where  $F$  denotes the Frobenius norm. This class is discussed in Subsection 2.1.

$$\sum_{i \in [0, n-1]} \|\mathbf{A}_i \mathbf{X} - \mathbf{ZB}_i\|_F^2 \quad (4)$$

However, in the first class of cost functions as given in Equation 4, we observed that artifacts and errors related to the calibration object and camera calibration method are sometimes propagated to the estimation of  $\mathbf{X}$  and  $\mathbf{Z}$ . The second class of cost functions aims to reduce the influence of these camera calibration artifacts by finding  $\mathbf{X}$  and  $\mathbf{Z}$  based on camera reprojection error, without explicitly using  $\mathbf{A}$  and this is discussed in Subsection 2.2.

Each of the aforementioned two classes of cost functions contains two or more sub-classes or methods, first, to explore different choices of cost functions; separable versus simultaneous solutions, and second, to explore different parameterizations of the rotation components. For the latter, we use three different possible parameterizations namely: Euler angles, axis-angle, and quaternions.

Since the two classes of cost functions are nonlinear, we use nonlinear least-square solvers based on the Levenberg-Marquardt method to find the approximate solutions of  $\mathbf{X}$  and  $\mathbf{Z}$ . It is important to mention here

that the above collection of classes and methods easily extend to the problem of calibrating multiple cameras mounted on one robot as shall be discussed in Subsection 2.3.

Similarities between the state-of-the-art and our proposed collection of methods are as follows. Our methods are iterative, like the method of Hirsh *et al.* [4] and the iterative method of Dornaika and Horaud [3]. The work of Malti [8] concerning using camera reprojection error to estimate HTMs  $\mathbf{X}$  and  $\mathbf{Z}$  is similar to our second class of methods, when using the Euler angle representation for rotations (Subsection 2.2). One difference is that Malti’s work assumes that the motions are relative and as a result uses different definitions of the matrices than we do.

Our contributions to the state-of-the-art in robot-world hand-eye calibration are summarized as follows:

- We provide a comprehensive comparison that explores different choices of cost function, parameter choices, and separable versus simultaneous solutions within our collection of methods, and contrast those methods with the state-of-the-art methods, on real datasets as well as on simulated datasets.
- Our collection of methods is provided to the community as open source code [14].

A portion of the work presented in this paper was previously published as [15]. However, the present paper expands the work of [15] in the following ways:

- This paper evaluates three different parameterizations of the rotation matrices in the experimental results: Euler angles, the axis-angle representation, and quaternions. Also, it discusses the effect of the parameter choice on results. In contrast, the prior work only used Euler angle parameterizations.
- While in [15] only simultaneous methods were proposed, we also created separable formulations of some of the cost functions and as a result were able to demonstrate the differences on the results produced by separability.
- We incorporated a comparison with the work of Shah [10], which was not presented in [15].
- Prior work only considered one camera. In contrast, the methods presented in this paper are generalized to the multiple-eye, one robot problem, with no limit to the number of cameras used.
- Four additional real datasets were acquired.
- Simulated datasets were added to the experiments, which allow comparisons between the estimated and true solutions and additional analysis of the methods.

## 2 Collection of methods description

Many of the differences among the previous methods concern how orthonormality of the rotation matrices is maintained. In this section, we first describe the parameterizations of the rotational components of  $\mathbf{X}$  and  $\mathbf{Z}$  such that orthonormality is preserved, and then discuss in details the two proposed classes of cost functions that we briefly introduced in the previous section followed by the extension to multiple cameras.

We explore three different parameterizations: Euler angle, axis-angle, and quaternions. Since these rotations are commonplace in the robotics literature and practice, in the next paragraph, we will only give a brief sketch of some details relevant to such parameterizations.

The Euler angle rotation representation is composed of three variables, which represent the rotation angles or direction cosines along the  $x, y, z$  directions. In this work, we selected the directional order of the rotations in the following order:  $x, y, z$ . Consequently, a rotation matrix can be represented as in the following manner  $\mathbf{R} = R_Z R_Y R_X$ . The axis-angle representation is another three-variable representation, where a three-element vector  $\mathbf{v}$  represents the axis of rotation, and  $\|\mathbf{v}\|$  is the angle of rotation about the  $\mathbf{v}$  axis such that a corresponding rotation matrix is generated with Rodrigues’ rotation formula. Finally, quaternions are a 4-element representation, where a unit vector  $\mathbf{q}$  can be converted to an orthonormal matrix.

We now define some notation to help us describe our two classes of cost functions and their extension to multiple cameras. Let the selected rotation representation be represented by a vector  $\mathbf{p}$ , with the size of  $\mathbf{p}$  equal to 3 for the Euler angles and the axis-angle representations, and equal to 4 for the quaternion representation. Then the directed cosine matrix representation of  $\mathbf{p}$  is  $\mathbf{R}(\mathbf{p})$ .

With these preliminaries, we will now present our first class of cost functions.

### 2.1 First class: $\mathbf{AX} = \mathbf{ZB}$

The first class of cost functions uses the world to camera transformations  $\mathbf{A}_i$  and base to end-effector transformations  $\mathbf{B}_i$  to estimate the HTMs  $\mathbf{X}$  and  $\mathbf{Z}$ . This is achieved by seeking the minimum of  $c_1$  as given below:

$$c_1 = \sum_{i=0}^{n-1} \|\mathbf{A}_i \mathbf{X} - \mathbf{Z} \mathbf{B}_i\|_F^2 \quad (5)$$

In the cost function  $c_1$  in Equation 5, if we substitute in the rotation representation  $\mathbf{R}(\mathbf{p})$  and the translation vectors for the unknowns  $\mathbf{X}$  and  $\mathbf{Z}$ , the minimization

problem becomes:

$$\operatorname{argmin}_{\mathbf{p}_X, \mathbf{t}_X, \mathbf{p}_Z, \mathbf{t}_Z} \sum_{i=0}^{n-1} \left\| \mathbf{A}_i \begin{bmatrix} \mathbf{R}(\mathbf{p}_X) & \mathbf{t}_X \\ \mathbf{0}^T & 1 \end{bmatrix} - \begin{bmatrix} \mathbf{R}(\mathbf{p}_Z) & \mathbf{t}_Z \\ \mathbf{0}^T & 1 \end{bmatrix} \mathbf{B}_i \right\|_F^2 \quad (6)$$

A solution to the problem in Equation 6 belongs to the simultaneous category of methods for robot-world hand-eye calibration, because the rotation and translation are solved for at the same time.

We can also break the minimization problem in Equation 6 into two parts via a separable formulation: one part for rotation and the other part to estimate the translation components as captured by Equation 7 and Equation 8, respectively.

$$\operatorname{argmin}_{\mathbf{p}_X, \mathbf{p}_Z} \sum_{i=0}^{n-1} \left\| \mathbf{R}_{A,i} \mathbf{R}(\mathbf{p}_X) - \mathbf{R}(\mathbf{p}_Z) \mathbf{R}_{B,i} \right\|_F^2 \quad (7)$$

$$\operatorname{argmin}_{\mathbf{t}_X, \mathbf{t}_Z} \sum_{i=0}^{n-1} \left\| \mathbf{R}_{A,i} \mathbf{t}_X + \mathbf{t}_A - \mathbf{R}(\mathbf{p}_Z) \mathbf{t}_{B,i} - \mathbf{t}_Z \right\|_F^2 \quad (8)$$

An approximate solution to Equation 7 is first found and then the translation components are found from Equation 8.

The left hand ( $\mathbf{A}\mathbf{X}$ ) and right hand ( $\mathbf{Z}\mathbf{B}$ ) sides of the cost function  $c_1$  represent the transformation from robot base to camera via the world coordinate system (left hand side) and from robot base to camera via the end-effector coordinate system (right hand side) as graphically captured in Figure 1. We also explore the use of a slightly different cost function  $c_2$  as given in Equation 9:

$$c_2 = \sum_{i=0}^{n-1} \left\| \mathbf{A}_i - \mathbf{Z}\mathbf{B}_i\mathbf{X}^{-1} \right\|_F^2 \quad (9)$$

We can find an approximate solution to  $c_2$  simultaneously, similar to what we did with the function  $c_1$ , by estimating  $\mathbf{p}_X$ ,  $\mathbf{t}_X$ ,  $\mathbf{p}_Z$ , and  $\mathbf{t}_Z$ . In order to simplify the notation, we let  $\tilde{\mathbf{X}} = \mathbf{X}^{-1}$ . Then  $\tilde{\mathbf{p}}_X$  and  $\tilde{\mathbf{t}}_X$  are the rotation parameters and translation vectors of  $\mathbf{X}^{-1}$ , respectively. With these substitutions, we have the following minimization problem:

$$\operatorname{argmin}_{\tilde{\mathbf{p}}_X, \tilde{\mathbf{t}}_X, \mathbf{p}_Z, \mathbf{t}_Z} \sum_{i=0}^{n-1} \left\| \mathbf{A}_i - \begin{bmatrix} \mathbf{R}(\mathbf{p}_Z) & \mathbf{t}_Z \\ \mathbf{0}^T & 1 \end{bmatrix} \mathbf{B}_i \begin{bmatrix} \mathbf{R}(\tilde{\mathbf{p}}_X) & \tilde{\mathbf{t}}_X \\ \mathbf{0}^T & 1 \end{bmatrix} \right\|_F^2 \quad (10)$$

As with  $c_1$ , it is possible to create a separable formulation by first estimating the rotation components in Equation 11 and then the translation components in Equation 12.

$$\operatorname{argmin}_{\tilde{\mathbf{p}}_X, \mathbf{p}_Z} \sum_{i=0}^{n-1} \left\| \mathbf{R}_{A,i} - \mathbf{R}(\mathbf{p}_Z) \mathbf{R}_{B,i} \mathbf{R}(\tilde{\mathbf{p}}_X) \right\|_F^2 \quad (11)$$

$$\operatorname{argmin}_{\tilde{\mathbf{t}}_X, \mathbf{t}_Z} \sum_{i=0}^{n-1} \left\| \mathbf{t}_{A,i} - \mathbf{R}(\mathbf{p}_Z) \mathbf{R}_{B,i} \tilde{\mathbf{t}}_X - \mathbf{R}(\mathbf{p}_Z) \mathbf{t}_B - \mathbf{t}_Z \right\|_F^2 \quad (12)$$

In both of the minimization formulations (simultaneous and separable) for  $c_1$  and  $c_2$ , the number of parameters to be estimated for  $\mathbf{X}$  and  $\mathbf{Z}$  are: six translation components and six or eight rotation parameters, depending on the choice of the rotation representation. Approximate solutions to all of the problems proposed in this paper are found with the Levenberg-Marquardt method for non-linear least squares [9] and specifically its implementation in *Ceres* [2]. For an initial solution, values are chosen such that  $\mathbf{R}(\mathbf{p}_X)$  and  $\mathbf{R}(\mathbf{p}_Z)$  are  $3 \times 3$  identity matrices and  $\mathbf{t}_X$  and  $\mathbf{t}_Z$  have all elements zero.

## 2.2 Second class: camera reprojection error

In this subsection, we present our second class of cost functions and methods, which are based on the idea of minimizing camera reprojection error in order to find  $\mathbf{X}$  and  $\mathbf{Z}$ . The approach presented in this subsection shares many similarities with the camera calibration approach of Zhang in [17], where the extrinsic camera calibration parameters are estimated by minimizing the camera reprojection error. Unlike the first class of methods, this approach is sensitive to the choice of initial solution; briefly, we use the result from the first class of methods as an initial solution and a more in-depth discussion of initial solution choices can be found in Subsection 3.1.

Before getting into the details of this class of methods, we first mention some preliminaries and notation. Let a three-dimensional point on the calibration object be  $\vec{\mathcal{X}}$ , and because there are multiple  $m$  such points we give a subscript  $j \in [0, m-1]$ ,  $\vec{\mathcal{X}}_j$ . It is assumed that all of the points are detected in the images used for calibration, so in the case of the chessboard pattern, these points are the corners of the chessboard. When  $\vec{\mathcal{X}}_j$  is projected to the image from robot position  $i$  using the intrinsic camera calibration parameters, we have image point  $\vec{\mathbf{x}}_{ij}$  and a corresponding original image point  $\vec{\mathbf{x}}_{ij}$ . We can represent  $\vec{\mathbf{x}}_{ij}$  in the context of the robot-world hand-eye calibration problem as follows:

$$\vec{\mathbf{x}}_{ij} = f(\mathbf{k}, [\mathbf{Z}\mathbf{B}_i\mathbf{X}^{-1}]_{3 \times 4} \vec{\mathcal{X}}_j) \quad (13)$$

where  $\mathbf{k}$  is a vector containing the intrinsic camera calibration parameters. The bracket notation  $[\ ]_{3 \times 4}$  is used to denote the upper  $3 \times 4$  sub-matrix of what is

inside the bracket.  $f()$  is the function that transforms  $[\mathbf{ZB}_i\mathbf{X}^{-1}]_{3\times 4}\vec{\mathcal{X}}_j$  into image points using  $\mathbf{k}$ .

Concerning  $\mathbf{k}$ , we use 4 parameters from the intrinsic camera calibration matrix and 8 radial and tangential distortion parameters, so  $|\mathbf{k}| = 12$ . However, other radial and tangential distortion models may be chosen with no change to the method. As with  $c_2$  in Equation 10, to simplify the representation of Equation 13, we substitute for  $\mathbf{X}^{-1}$  another matrix  $\tilde{\mathbf{X}}$ , which is composed of an orthonormal rotation matrix and translation vector.

Given the preliminaries discussed above, the reprojection sum of squares error ( $rsse$ ) is:

$$rsse = \sum_{i=0}^{n-1} \sum_{j=0}^{m-1} \|\vec{\mathbf{x}}_{ij} - \vec{\tilde{\mathbf{x}}}_{ij}\|^2 \quad (14)$$

and by substituting  $\vec{\tilde{\mathbf{x}}}_{ij}$  we have:

$$rsse = \sum_{i=0}^{n-1} \sum_{j=0}^{m-1} \|\vec{\mathbf{x}}_{ij} - f(\mathbf{k}, [\mathbf{ZB}_i\tilde{\mathbf{X}}]_{3\times 4}\vec{\mathcal{X}}_j)\|^2 \quad (15)$$

We note that in Equations 14 and 15 and for the remainder of this paper, we use the L2 norm for vectors.

Finally, if we substitute in the rotation representation  $\mathbf{R}(\mathbf{p})$  and the translation vectors for the unknown  $\tilde{\mathbf{X}}$  and  $\mathbf{Z}$  matrices, the camera reprojection sum of squares error ( $rsse$ ) minimization problem becomes as given in Equation 16, which we refer to as  $rp_1$  method:

$$\underset{\tilde{\mathbf{p}}_X, \tilde{\mathbf{t}}_X, \mathbf{p}_Z, \mathbf{t}_Z}{\operatorname{argmin}} \sum_{i=0}^{n-1} \sum_{j=0}^{m-1} \|\vec{\mathbf{x}}_{ij} - f(\mathbf{k}, \begin{bmatrix} \mathbf{R}(\mathbf{p}_Z) & \mathbf{t}_Z \\ \mathbf{0}^T & 1 \end{bmatrix} \mathbf{B}_i \begin{bmatrix} \mathbf{R}(\tilde{\mathbf{p}}_X) & \tilde{\mathbf{t}}_X \\ \mathbf{0}^T & 1 \end{bmatrix} \vec{\mathcal{X}}_j)\|^2 \quad (16)$$

where  $\tilde{\mathbf{p}}_X$  and  $\tilde{\mathbf{t}}_X$  are again the rotation parameter vector and translation vectors of  $\tilde{\mathbf{X}}$  or  $\mathbf{X}^{-1}$ , respectively.

Within the simultaneous formulation of the robot-world hand-eye calibration problem as given in Equation 16, it is also possible to refine the camera intrinsic parameter vector  $\mathbf{k}$  by letting  $\mathbf{k}$  be parameters to be estimated in order to produce a local minimum in Equation 16 instead of constants as given in Equation 17, which we refer to as the  $rp_2$  method.

$$\underset{\tilde{\mathbf{p}}_X, \tilde{\mathbf{t}}_X, \mathbf{p}_Z, \mathbf{t}_Z, \mathbf{k}}{\operatorname{argmin}} \sum_{i=0}^{n-1} \sum_{j=0}^{m-1} \|\vec{\mathbf{x}}_{ij} - f(\mathbf{k}, \begin{bmatrix} \mathbf{R}(\mathbf{p}_Z) & \mathbf{t}_Z \\ \mathbf{0}^T & 1 \end{bmatrix} \mathbf{B}_i \begin{bmatrix} \mathbf{R}(\tilde{\mathbf{p}}_X) & \tilde{\mathbf{t}}_X \\ \mathbf{0}^T & 1 \end{bmatrix} \vec{\mathcal{X}}_j)\|^2 \quad (17)$$

In contrast with the minimized reprojection sum of squared error ( $rsse$ ) in both  $rp_1$  and  $rp_2$  methods,

it is important to mention that in the camera calibration literature, the reprojection root mean squared error ( $rrmse$ ) is more common, as shown in Equation 18. The  $rrmse$  represents the average Euclidean distance between detected and reprojected calibration pattern points in the image plane, and its units are pixels. However, since the parameters that result in a minimum of  $rsse$  also result in a minimum of  $rrmse$ ,  $rsse$  is used as a cost function in this work.

$$rrmse = \sqrt{\frac{1}{mn} \sum_{i=0}^{n-1} \sum_{j=0}^{m-1} \|\vec{\mathbf{x}}_{ij} - \vec{\tilde{\mathbf{x}}}_{ij}\|^2} \quad (18)$$

### 2.3 Extending the two proposed classes of methods to multiple cameras

The multiple camera case requires estimating one HTM  $\mathbf{X}$  and multiple HTMs  $\mathbf{Z}$ . As such, if we let the number of cameras be  $q$ , and  $\mathbf{A}_{i,0}$  be the transformation from the world coordinate frame to the  $0^{\text{th}}$  camera at the  $i^{\text{th}}$  robot position. Then the relationship between the matrices in the context of robot-world hand-multiple-eyes calibration problem would be formulated as:

$$\mathbf{A}_{i,0}\mathbf{X} = \mathbf{Z}_0\mathbf{B} \quad (19)$$

$$\mathbf{A}_{i,1}\mathbf{X} = \mathbf{Z}_1\mathbf{B} \quad (20)$$

⋮

$$\mathbf{A}_{i,q-1}\mathbf{X} = \mathbf{Z}_{q-1}\mathbf{B} \quad (21)$$

for all  $i \in [0, n-1]$ . Therefore, we should now be able to represent all of the cost functions presented thus far in Subsections 2.1 and 2.2 within this multiple camera context. For instance, Equation 6 in the multiple camera context becomes:

$$\underset{\mathbf{p}_X, \mathbf{t}_X, \mathbf{p}_{Z,0}, \mathbf{t}_{Z,0}, \mathbf{p}_{Z,1}, \mathbf{t}_{Z,1}, \dots, \mathbf{p}_{Z,q-1}, \mathbf{t}_{Z,q-1}}{\operatorname{argmin}} \sum_{d=0}^{q-1} \sum_{i=0}^{n-1} \left\| \mathbf{A}_{i,d} \begin{bmatrix} \mathbf{R}(\mathbf{p}_X) & \mathbf{t}_X \\ \mathbf{0}^T & 1 \end{bmatrix} - \begin{bmatrix} \mathbf{R}(\mathbf{p}_{Z,d}) & \mathbf{t}_{Z,d} \\ \mathbf{0}^T & 1 \end{bmatrix} \mathbf{B}_i \right\|_F^2 \quad (22)$$

where  $\mathbf{p}_{Z,d}$  and  $\mathbf{t}_{Z,d}$  are the rotation parameterization and translation vectors for the  $d^{\text{th}}$  HTM,  $\mathbf{Z}_d$ . Separable versions follow using the same pattern, as it is done in the cost function  $c_1$  and the  $rsse$  formulations of the two classes of methods found in the previous subsections.

When using multiple cameras, it is common that in order to gain a wide variety of views of the calibration object, not all images for each camera will view the calibration object, particularly if the cameras are far apart or have different lenses and imaging sensor sizes. We now describe a generic method that we used

in our implementation, to weight the influences from each camera in the cost function. We desired that each camera have an equal influence, but this weighting can be adjusted according to other needs.

We let the set of robot positions where a camera  $d$  can view the calibration object be  $\mathbb{S}_d$ , and denote  $min_s$  as the minimum size of  $\mathbb{S}_d$  determined for all cameras. Then, an individual weight  $w_d$  for camera  $d$  can be set as  $\frac{min_s}{|\mathbb{S}_d|}$ . Furthermore, if we let the cost function that is to be minimized be  $g()$ , the formulation of the robot-world hand-multiple-eyes calibration problem such that missing observations are handled is given by Equation 23.

$$\underset{\substack{\mathbf{p}_X, \mathbf{t}_X, \\ \mathbf{p}_{Z,0}, \mathbf{t}_{Z,0}, \\ \mathbf{p}_{Z,1}, \mathbf{t}_{Z,1}, \\ \dots \\ \mathbf{p}_{Z,q-1}, \mathbf{t}_{Z,q-1}}}{\text{argmin}} \sum_{d=0}^{q-1} \sum_{i \in \mathbb{S}_d} w_d g(\mathbf{p}_X, \mathbf{t}_X, \mathbf{p}_{Z,d}, \mathbf{t}_{Z,d}) \quad (23)$$

The problem in Equation 23 can be applied to the first class of cost functions, as well as the *rp1* method in the second class of methods. For the *rp2* method in the second class of cost functions, we also estimate intrinsic camera calibration parameters  $\mathbf{k}$  for all  $q$  cameras and doing so follows from Equation 23.

### 3 Performance Evaluation on real datasets

The behavior of the robot-world hand-eye calibration methods is demonstrated on eight datasets in real laboratory and field settings.<sup>1</sup> These datasets represent different combinations of robots, cameras, and lenses; some of the datasets have multiple cameras. Descriptions of the datasets are given in Table 1. The table also lists the number of robot positions ( $n$ ) used for the calibration and the *rrmse* error (in pixels) from the camera calibration step using Zhang’s method [17] to estimate the matrices  $\mathbf{A}_i$ . For datasets 7 and 8, the third camera is a commodity RGB-D (Red-Green-Blue-Depth) camera; we calibrated only the color camera in this work. Figure 2 shows the arrangement of cameras in dataset 7 as well as sample images from one position of the robot. Figure 3 shows both of the robots used in this work; two 6-axis robot arms were used, a Denso VS-6577GM-B robot arm rigidly mounted to the floor and a Denso VM-60BIG robot arm mounted on a mobile platform.

In the rest of this section, we discuss some of the implementation details of our collection of proposed methods, and then discuss the error metrics used in

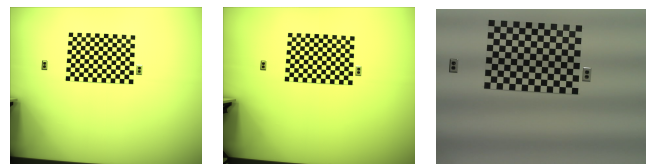
reporting the performance results of the comparison of the proposed methods.

**Table 1** Dataset descriptions. The number of robot positions is  $n$ , and *rrmse* is the reprojection root mean square error from the camera calibration step.

Dataset	Image Size	Lens focal length	Robot	$n$	<i>rrmse</i> [pixels]
1	(640 × 480)	8mm	Denso VS-6577GM-B	88	0.185242
2	(2456 × 2058)	8mm	Denso VS-6577GM-B	28	0.199418
3	(2456 × 2058)	6mm	Denso VM-60BIG	36	0.540056
4	(1600 × 1200)	6mm	Denso VM-60BIG	20	0.447463
5	(1228 × 1029)	6mm	Denso VS-6577GM-B	15	0.124774
6	(1228 × 1029)	6mm	Denso VS-6577GM-B	15	0.124774
	(1228 × 1029)	6mm			0.118215
7	(1228 × 1029)	6mm	Denso VS-6577GM-B	42	0.131076
	(1228 × 1029)	6mm			0.121817
	(640 × 480)	not provided			0.109997
8	(1228 × 1029)	8mm	Denso VS-6577GM-B	42	0.143151
	(1228 × 1029)	8mm			0.139296
	(640 × 480)	not provided			0.113589



(a) The arrangement of cameras in dataset 7



(b) Camera 0

(c) Camera 1

(d) Camera 2

**Fig. 2** An example of the experimental setup for dataset 7, consisting of three cameras and the images from each camera for one stop of the robot

#### 3.1 Implementation details

For the two proposed classes of cost functions, we use the implementation of the Levenberg-Marquardt method found in the software package *Ceres* [2]. All of the results shown in this paper were generated on a workstation with one 12-core processor and 192 GB of RAM. The camera calibration was carried out using the OpenCV library’s camera calibration functions [1].

For the first class of cost functions using simultaneous and separable versions of  $c_1$  and  $c_2$ , the initial

<sup>1</sup> All of the datasets are available from [14].



(a) Denso VS-6577GM-B



(b) DENSO VM-60BIG

**Fig. 3** Two 6-axis robot arms used to generate the performance evaluation datasets. In Subfigure 3a, three cameras are mounted on the end-effector as in dataset 7, and this robot arm is rigidly attached to the laboratory floor. Subfigure 3b shows the larger robot arm mounted on a mobile platform with one camera (Subfigure 3b image is courtesy of Edwin Winzeler).

solutions of  $\mathbf{p}_X$  and  $\mathbf{p}_Z$  are set such that the corresponding directed cosine matrix is a  $3 \times 3$  identity matrix, and the translation components are set to zero.<sup>2</sup> As mentioned previously, the second class of cost functions  $rp_1$  and  $rp_2$  are sensitive to initial solutions. To find an approximate solution to the minimization problem of  $rp_1$  method that was shown in Equation 16, we used the simultaneous solution using the  $c_2$  cost function (problem specified in Equation 10) as an initial solution. To find an approximate solution to the problem of the  $rp_2$  method shown in Equation 17, the solution from Equation 16 was used as the initial solution.

To present a comparative study against our collection of cost functions and methods, we implemented

<sup>2</sup> Various different initial solutions were tested, and there was small or negligible difference in the solution quality versus using an identity matrix for rotation matrices and translation component with all elements zero. For this reason, we conclude that for the experiments covered in this paper, the first class of methods is not sensitive to initial solutions.

seven comparison methods: Zhuang *et al.* [18], Dornaika and Horaud [3]: closed form and iterative, Hirsh *et al.* [4] and Li *et al.* [6] based on the dual quaternion and Kronecker product, and the work of Shah [10]. Concerning the implementation details of Li *et al.* [6] methods, we draw the reader's attention that the computation of coefficients  $\lambda_1$  and  $\lambda_2$  in the dual quaternion method was not specified clearly by the authors, thus we used a Levenberg-Marquardt method to find those values. For the conversion of rotation matrices found by the Kronecker product method [6] into orthonormal matrices, we used the singular value decomposition method.

### 3.2 Error metrics

In presenting the comparison results of both of our collection of methods and those methods of others, we used the following error metrics: two types of mean rotation error, the mean translation error, the mean combined rotation and translation error, and the reprojection root mean squared error. Since we are interested in using our methods for reconstruction and vision tasks as indicated in Subsection 1.2, we also introduced a sixth metric related to reconstruction accuracy. The following subsections describe each error type.

#### 3.2.1 The Mean Rotation Error

We list two rotation errors. The first, which we denote Rotation Error 1 ( $e_{R1}$ ), is derived from Equation 2 and shown in Equation 24.

$$e_{R1} = \frac{1}{n} \sum_{i=0}^{n-1} \|\mathbf{R}_{A_i} \mathbf{R}_X - \mathbf{R}_Z \mathbf{R}_{B_i}\|_F^2 \quad (24)$$

However, the  $e_{R1}$  value may not be particularly meaningful when evaluating the methods, and has no units. For this reason, we have a second rotation error,  $e_{R2}$ , that is representative of the difference between the left hand and right hand sides of Equation 2. We find the relative rotation between the two sides (Equation 25) and then compute the angle of the relative rotation using the axis-angle representation, which is represented as  $angle()$  in Equation 26; in the results shown in Section 5, its units are degrees.

$$\mathbf{R}_i = (\mathbf{R}_Z \mathbf{R}_{B_i})^T (\mathbf{R}_{A_i} \mathbf{R}_X) \quad (25)$$

$$e_{R2} = \frac{1}{n} \sum_{i=0}^{n-1} angle(\mathbf{R}_i) \quad (26)$$



### 3.2.2 The Mean Translation Error

The translation error is derived from Equation 3 and shown in Equation 27, where the units are in millimeters to be consistent with our selection of units for camera calibration error.

$$e_t = \frac{1}{n} \sum_i \|(\mathbf{R}_{A_i} \mathbf{t}_X + \mathbf{t}_{A_i}) - (\mathbf{R}_{Z_i} \mathbf{t}_B + \mathbf{t}_{Z_i})\|^2 \quad (27)$$

### 3.2.3 The Mean Combined Rotation and Translation Error

This error is shown in Equation 28 and has no units.

$$e_C = \frac{1}{n} \sum_i \|\mathbf{A}_i \mathbf{X} - \mathbf{Z} \mathbf{B}_i\|_F^2 \quad (28)$$

### 3.2.4 The Reprojection Root Mean Squared Error (*rrmse*)

This error is shown in Equation 29 and its units are pixels.

$$rrmse = \sqrt{\frac{1}{mn} \sum_{i=0}^{n-1} \sum_{j=0}^{m-1} \|\vec{\mathbf{x}}_{ij} - f(\mathbf{k}, [\mathbf{Z} \mathbf{B}_i \mathbf{X}^{-1}]_{3 \times 4} \vec{\mathbf{x}}_j)\|^2} \quad (29)$$

### 3.2.5 The Reconstruction Accuracy Error

Since we are also interested in reconstruction accuracy when using a robot to acquire images with associated camera calibration information, our final metric aims to represent the reconstruction accuracy.

The idea behind this metric is given correspondences from different images acquired at different robot positions, estimate the world points that generated those correspondences, and compute the difference between the estimated versus true world points to represent reconstruction accuracy. We borrow some of the notation from Section 2.2:  $\vec{\mathbf{x}}_{ij}$  is the  $j$ th image point from the  $i$ th robot position and corresponds to the three-dimensional point  $\vec{\mathbf{x}}_j$ . First, we estimate the most likely three-dimensional point (represented by  $\hat{\mathcal{Y}}_j$ ) that generated the  $n$   $\vec{\mathbf{x}}_{ij}$  image points by solving the minimization problem in Equation 30.

$$\hat{\mathcal{Y}}_j = \operatorname{argmin}_{\mathcal{Y}_j} \sum_{i=0}^{n-1} \|\vec{\mathbf{x}}_{ij} - f(\mathbf{k}, [\mathbf{Z} \mathbf{B}_i \mathbf{X}^{-1}]_{3 \times 4} \mathcal{Y}_j)\|^2 \quad (30)$$

Then, the reconstruction accuracy error (*rae*) is the average Euclidean distance between the estimated  $\hat{\mathcal{Y}}_j$  points and calibration object points  $\vec{\mathbf{x}}_j$ :

$$rae = \frac{1}{m} \sum_{j=0}^{m-1} \|\hat{\mathcal{Y}}_j - \vec{\mathbf{x}}_j\|^2 \quad (31)$$

## 4 Performance Evaluation on simulated datasets

The comparison methods as well as a subset of our proposed methods are evaluated on simulated datasets. For the simulated datasets contained in this paper, only  $\mathbf{A}_i$ ,  $\mathbf{B}_i$ ,  $\mathbf{X}$ , and  $\mathbf{Z}$  are generated. As a result, we do not evaluate our proposed second class of methods, since doing so would also require simulating camera models. The protocol for generating the simulated datasets closely follows that of Shah 2013 [10], Section 5.1. Briefly, the rotation components of  $\mathbf{A}_i$ ,  $\mathbf{X}$ , and  $\mathbf{Z}$  are set as random rotation matrices, and the translation components are drawn from the standard uniform distribution (0,1) using a random number generator, for  $i = 1, 2, \dots, 25$ . Then, the homogeneous matrix  $\mathbf{B}_i$  is computed as:

$$\mathbf{B}_i = \mathbf{Z}^{-1} \mathbf{A}_i \mathbf{X} \quad (32)$$

Noise is then introduced to  $\mathbf{B}_i$ , only in the rotation component, by converting the rotation matrix to the quaternion representation and adding random noise, and then converting back to the matrix representation.  $\eta$  is the parameter controlling the magnitude of the random noise added to  $\mathbf{B}_i$ .  $\eta \in (0, 0.25]$  and is evenly spaced over 19 values along that interval. Data was generated for ten trials of the experiment.

The protocol above sets the translation components within the interval of (0,1), which reflects a bias towards a particular use of units. Depending on the particular experiment setup and choices made, this interval may or may not be representative of that experimental setup. Consequently, we denote the simulated datasets using Shah's protocol [10] as Simulated Dataset I. We generated another dataset using the same protocol, except that the translation components were within the interval of (0,1000), and refer to this as Simulated Dataset II. We chose the interval (0,1000) since in our real experiments we use millimeters for translation components to be consistent with camera calibration; of course, the use of meters would be another choice and this choice is reflected in Simulated Dataset I.

#### 4.1 Error metrics for simulated datasets

Since the ground truth  $\mathbf{X}$  and  $\mathbf{Z}$  are known for the simulated datasets, for each calibration method the difference between the rotation and translation components are computed. Again, we follow closely Shah’s presentation [10] in our description of the error metrics for the simulated experiments.

##### 4.1.1 Rotation error

Let  $\hat{\mathbf{R}}_X$  be the rotation matrix estimated by a calibration method for a simulated dataset, and  $\mathbf{R}_X$  be the ground truth rotation matrix for  $\mathbf{X}$ . Then, the error in the rotation component is  $e_{RX}$ :

$$e_{RX} = \|\hat{\mathbf{R}}_X - \mathbf{R}_X\|_F \quad (33)$$

and the same formula follows to compute the rotation error for  $\mathbf{Z}$ ,  $e_{RZ}$ .

##### 4.1.2 Translation error

Let  $\hat{\mathbf{t}}_X$  be the translation vector estimated by a calibration method for a simulated dataset, and  $\mathbf{t}_X$  be the ground truth translation vector for  $\mathbf{X}$ . Then, the error in the translation component is  $e_{tX}$ :

$$e_{tX} = \|\hat{\mathbf{t}}_X - \mathbf{t}_X\| \quad (34)$$

and the same formula follows to compute the translation error for  $\mathbf{Z}$ ,  $e_{tZ}$ .

## 5 Experimental Results

In this section, we first show and discuss comparison results between our methods and the seven methods we referred to in the previous section on real datasets. Then, we show and discuss comparison results using the two simulated datasets.

Tables 2 through 9 show the results using the five error metrics described in Subsection 3.2 and the eight real datasets described in Table 1.<sup>3</sup> These comparison results also include the running time for our implementation of each method in seconds.

In Tables 2 – 6, the first seven rows correspond to the seven comparison methods from the literature, listed in chronological order: Zhuang *et al.* [18], Dornaika and Horaud [3]: closed form and iterative, Hirsh *et al.* [4] and Li *et al.* [6] based on the dual quaternion

<sup>3</sup> While use of tables is perhaps not the easiest for the reader, we note that the huge range of values for each of the six error metrics made other types of representation (graphs, etc.) infeasible.

and Kronecker product, and the method of Shah [10], whereas the remainder of the rows correspond to our proposed methods.<sup>4</sup> The comparison methods were not evaluated on Datasets 6, 7, and 8 and are not shown in Tables 7 - 9, because those datasets have more than one camera, and to the best of our knowledge, there are currently no other robot-world hand-eye calibration methods for multiple cameras.

Results for Simulated Datasets I and II are shown graphically in Figures 4 - 7. The seven comparison methods were evaluated as well as the first class from our proposed collection of methods. Within the first class of our proposed collection of methods, the results were very similar for different choices of rotation parameterization. Consequently, we only listed one rotation parameterization choice, that of Euler angles, to allow better readability.

#### 5.1 Discussion of comparison methods on real datasets

We mention here that the Dornaika and Horaud iterative method [3] does not converge for any datasets using the *Ceres* solver [2], where derivatives are automatically computed by the software. In comparison, in our previous work [15], where we used the *levmar* solver [7], the Dornaika and Horaud iterative method converged after only 2-3 iterations after termination conditions were met, however, the results were very similar to that produced with the authors’ closed form method (which served as the iterative method’s initial solution). In summary, the behavior of different solvers may give different results, but the main conclusion we have made about this method is that the large penalty terms used to enforce orthonormality of the rotation matrices result in either very little change from the initial solution, or non-convergent behavior.

Another similarity among the comparison methods is the Hirsh *et al.* [4] and Shah [10] methods. Both of these methods consistently produce the lowest values of rotation errors  $e_{R1}$  and  $e_{R2}$  that are usually the same up to 5 digits of precision. In contrast, the Dornaika and Horaud closed-form method [3] usually has one of the highest rotation errors. With regard to the mean translation error ( $e_t$ ) and the combined rotation and translation error ( $e_C$ ), Shah’s method in general has a good performance relative to other comparisons methods as it results in one of the lowest values among the datasets until Dataset 5 (Table 6). With respect to the reprojection mean square error (*rrmse*), the Hirsh *et al.* [4] and Shah [10] methods both perform generally

<sup>4</sup> Only the first author is mentioned in the tables’ text for brevity.

the best, with Shah’s method resulting in lower *rrmse* in general as compared to the method of Hirsh *et al.*, though this relationship is inverted in Datasets 1 and 5. For example, the method of Hirsh *et al.* has the lowest *rrmse* in Datasets 1 (3.68829 pixels), but large *rrmse* in Dataset 5 (238.041 pixels), though still lower compared to Shah’s method’s *rrmse* value (439.512 pixels).

The first conclusion drawn from Tables 2 – 6, which correspond to datasets with a single camera, is that the behavior of many methods is dataset dependent. This dataset dependency may result from many factors, including the positions chosen for calibration, the robot model, and the way in which the robot is mounted, which may introduce new errors. Recall from Section 3 that the DENSO VM-60BIG from Datasets 3 and 4 is mounted on a mobile unit with tires, so as the robot moves, there might be some movement in the robot base.

The dataset dependency of the comparison methods is illustrated with a selection of examples. For instance, the combined rotation and translation error ( $e_C$ ) of Zhuang *et al.* [18] is the lowest of the group of comparison methods in Dataset 1 (233.3), in the middle range in Dataset 2, and greater than 170,000 in Datasets 3, 4, and 5. The Kronecker product method from Li *et al.* [6] performed well relative to the comparison methods for Dataset 5 (Table 6), where the combined rotation and translation error was  $e_C = 329.24$  and the other methods had combined rotation and translation error  $e_C \geq 13,000$ . However, for no other single dataset that has one camera does the Li *et al.* Kronecker product method have the lowest combined rotation and translation error relative to the other comparison methods.

## 5.2 Discussion of the proposed collection of methods on real datasets

### 5.2.1 First class of cost functions

Within the first class of cost functions, the methods based on minimizing  $c_1$  (*i.e.* simultaneous and separable under different choices of parameterization of the rotational components) tend to have a lower value of combined rotation and translation error ( $e_C$ ), while methods based on minimizing  $c_2$  have lower values of *rrmse* as compared to  $c_1$  methods. Exceptions are Datasets 7 and 8, which have very similar values of  $e_C$  and *rrmse* for  $c_1$  and  $c_2$  separable versions (see Tables 8 and 9).

Specifically, within the first class of cost functions, the separable versions of the methods tended to have lower rotation errors  $e_{R1}$ ,  $e_{R2}$ , but higher translation errors  $e_t$  and combined rotation and translation error  $e_C$ , as well as reprojection error *rrmse*. This is particularly

obvious in Dataset 5 (Table 6), where the reprojection root mean square errors of the separable versions are all greater than 48 pixels, while the simultaneous versions have a maximum *rrmse* of 3.89 pixels. The separable methods have a much greater *rrmse* than the simultaneous versions in particular in Dataset 6, Table 7.

### 5.2.2 Second class of cost functions

As expected when using reprojection error as a cost function versus the relationship  $\mathbf{AX} = \mathbf{ZB}$  (and its variations), the second class of methods consistently gives results with lower values of *rrmse* than the first class of methods or the comparison methods. On the other hand, the rotation errors, translation errors and combined rotation and translation errors, when using the second class of methods, are greater than the first class of methods as well as some of the comparison methods. In general, the change in *rrmse* using  $rp_1$  (where intrinsic camera calibration parameters are treated as constants) versus  $rp_2$  (where intrinsic camera calibration values are parameters) is small.

### 5.2.3 Effect of rotation representation

It seems that the choice of rotation representation – Euler angles, axis-angle, or quaternion – has only a small effect on the results, and those differences may be dependent on the particular solver used. For instance, in our prior work [15], the simultaneous version of the cost function  $c_1$  was used based on the Euler angles parameterization (in that work, labeled as Euler Parameterization I) using the *levmar* solver [7] and a provided Jacobian matrix. In that work, when tested on Dataset 1, the *rrmse* was 3.62709 pixels. Whereas using the *Ceres* solver [2] with automatic Jacobian matrices for the same dataset, the *rrmse* values were 12.13, 3.62686 and 3.62641 pixels, respectively for the Euler angles, axis-angle and quaternion versions (Table 2). This difference in *rrmse* occurs even in the cases when the combined rotation and translation error ( $e_C$ ) between the three rotation representations, using *Ceres*, differs by only 0.001. Usually, the differences between the rotation representations on all of the metrics are relatively small, though exceptions are Datasets 5 and 6 (Tables 6 and 7), the separable  $c_1$  and  $c_2$  methods.

## 5.3 Reconstruction accuracy performance for the proposed collection of methods and comparison methods

While reprojection root mean square error is a good indicator of relative reconstruction accuracy error (*rae*),

there is not a monotonic relationship of  $rrmse$  to  $rae$ . We observed that the  $rp_2$  version from the second class in our collections returns slightly lower values of  $rrmse$  than  $rp_1$ . Concerning reconstruction accuracy error of the  $rp_2$  method versus the  $rp_1$  method,  $rae$  increases slightly in datasets with better selections of robot positions (Datasets 1, 2, 3, 4, 7, 8) using  $rp_1$  and decreases slightly in datasets with poorer selections of robot positions (Datasets 5 and 6) when using  $rp_2$  method as compared to the  $rp_1$  method. Concerning our first class of cost functions ( $c_1$  and  $c_2$ ), we observed that using the  $c_2$  simultaneous method always gives a lower  $rae$ . In particular, the  $c_2$  simultaneous version in Dataset 2 has  $rae \leq 0.1$  mm for all three rotation representations, and this pattern ( $rae \leq 0.1$  mm) is repeated in the separable versions of  $c_2$  as compared to  $c_1$  ( $rae \leq 15$  mm,  $rae \leq 2.38$  mm for separable and simultaneous, respectively). Additionally, it is observed that the separable versions of both  $c_1$  and  $c_2$  perform well in some datasets with respect to  $rae$  and worse in others (e.g. perform well in Dataset 2 ( $rae \leq 2.381$  mm), and perform poorly in Dataset 5 ( $rae \geq 33,338.9$  mm)).

Within the group of comparison methods, the methods of Hirsh *et al.* [4] and Shah [10] consistently have the lowest values of rotation error, and both of these methods perform generally well with respect to  $rrmse$ . In general, Shah’s computation of translation vectors results in lower translation error ( $e_t$ ) and  $rrmse$  as compared to the method of Hirsh *et al.*, though this relationship is inverted in Dataset 5. However, none of the comparison methods performs as well as our proposed  $rp_1$  and  $rp_2$  methods with respect to reconstruction accuracy error, though for some datasets the methods of Hirsh *et al.* and Shah are comparable to the  $rae$  of our first class of proposed methods.

#### 5.4 Discussion of the simulated experiments

The examination of the Simulated Dataset I and II results offer some additional insights into the behavior of the comparison and proposed methods, since the ground truth  $\mathbf{X}$  and  $\mathbf{Z}$  are known. The Simulated Dataset I results for the rotation error for  $\mathbf{X}$  and  $\mathbf{Z}$ , show that the Shah and Li *et al.* Kronecker product methods consistently producing the rotation matrices closest to the ground truth, while the rest of the methods have very similar error values ranging from 2 and 2.6. The Shah and Li *et al.* Kronecker product methods also have the lowest translation error for  $\mathbf{X}$  and  $\mathbf{Z}$  in Simulated Dataset I, while the rest of the methods have similar error values. One exception is the Li *et al.* dual quaternion method, which has the largest error than the rest

of the methods for the translation components of  $\mathbf{X}$  and  $\mathbf{Z}$ .

Simulated Dataset II is different from Simulated Dataset I in the scaling of the translation components, and this difference affects the performance of the methods. Concerning rotation error, as before the Shah and Li *et al.* Kronecker product methods produce the lowest values, but in Simulated Dataset II the simultaneous versions from our first class of proposed methods also produce comparable values. For translation error, the Li *et al.* Kronecker product and simultaneous versions from our first class of proposed methods produce very low error values ( $\leq 0.061$ ), while the remainder have values which vary considerably.

From these experiments, it is clear that some methods are sensitive to the scaling and distribution of the translation components, and a different method for dataset generation may yield different observations. The Li *et al.* Kronecker product method seems to be a robust choice in both of these settings, the Shah method for the Simulated Dataset I setting, and our first class of proposed methods for the Simulated Dataset II setting.

#### 5.5 Recommendations and Summary

When choosing a robot-world, hand-eye calibration method to use, we hope that our experiments can aid researchers choose the method best suited to a particular task or application. For instance, the methods of Hirsh *et al.* [4] and Shah [10], and the  $c_1$  and  $c_2$  separable versions from the first class of our proposed methods consistently give the lowest rotation errors, whereas the  $c_1$  simultaneous method returns the lowest combined rotation and translation error  $e_C$ . For the best  $rrmse$  and  $rae$  without using camera reprojection error in the cost function, the  $c_2$  simultaneous method is the best choice. When using camera reprojection error as the cost function,  $rp_1$  is generally better on  $rae$  with a higher quality camera calibration and  $rp_2$  is better than  $rp_1$  with a poorer quality intrinsic camera calibration. Within the collection of methods we propose, the choice of rotation representation does not greatly affect the results when using a modern solver such as Ceres [2].

## 6 Conclusions

We presented a collection of methods for robot-world hand-eye calibration (including the case of multiple cameras) with accompanying code. Within this collection, we explored cost functions related to the equality  $\mathbf{AX} = \mathbf{ZB}$  (including simultaneous and separable versions) and camera reprojection error. We also implemented these

**Table 2** Comparison of methods using the error metrics described in Section 3.2 for Dataset 1.

Method	Time (s)	$e_{R1}$	$e_{R2}$ (degrees)	$e_t$ (mm)	$e_C$	$rrmse$ (pixels)	$rac$ (mm)
Zhuang [18]	0.025	0.000101190	0.336407	1.62805	233.3	4.35341	434.012
Dornaika [3]: Closed Form	0.01	0.261051	19.5162	61.24160	330047	762.333	195437.640
Dornaika [3]: Iterative	3.464	1.947	58.652	56.7113	283025	272.697	231374.732
Hirsh [4]	2.273	0.000098372	0.331641	2.02068	359.3	3.68820	189.545
Li [6]: Dual Quaternion	0.494	0.000174349	0.506214	1.90747	320.2	4.30692	103.749
Li [6]: Kronecker product	0.005	0.000102497	0.347818	2.25149	446.1	5.41810	388.55
Shah [10]	0.001	0.000098372	0.331641	1.63616	235.577	4.10190	403.674
<b><math>c_1</math>, Euler angles, simultaneous</b>	0.524	0.0002675	0.622864	1.56439	215.365	12.13	772.895
<b><math>c_1</math>, axis angle, simultaneous</b>	0.435	0.000108493	0.364398	1.56439	215.364	3.62686	268.006
<b><math>c_1</math>, quaternion, simultaneous</b>	0.458	0.000108522	0.364739	1.56439	215.364	3.62641	266.815
<b><math>c_2</math>, Euler angles, simultaneous</b>	0.511	0.000111989	0.367257	1.77959	278.692	1.67244	5.82014
<b><math>c_2</math>, axis angle, simultaneous</b>	0.423	0.00010333	0.350712	1.72619	262.215	1.66791	5.01893
<b><math>c_2</math>, quaternion, simultaneous</b>	0.556	0.000103324	0.350664	1.72618	262.215	1.66771	5.00157
<b><math>c_1</math>, Euler angles, separable</b>	1.54	0.0000983715	0.331638	1.63597	235.524	4.09968	403.114
<b><math>c_1</math>, axis angle, separable</b>	0.981	0.0000983714	0.331641	1.63614	235.573	4.10055	403.335
<b><math>c_1</math>, quaternion, separable</b>	2.01	0.0000983715	0.331634	1.63566	235.433	4.09923	403.33
<b><math>c_2</math>, Euler angles, separable</b>	1.331	0.0000983714	0.331642	1.75085	269.761	2.29073	5.64685
<b><math>c_2</math>, axis angle, separable</b>	0.868	0.0000983714	0.331637	1.75079	269.745	2.29095	5.645626
<b><math>c_2</math>, quaternion, separable</b>	0.895	0.0000983714	0.331642	1.75099	269.806	2.29097	5.661261
<b><math>rp_1</math>, Euler angles</b>	14.548	0.000127916	0.384648	1.96216	338.808	1.56905	0.2382108
<b><math>rp_1</math>, axis angle</b>	15.507	0.000127963	0.384498	1.96183	338.691	1.56905	0.2373199
<b><math>rp_1</math>, quaternion</b>	15.622	0.000127963	0.384498	1.96183	338.691	1.56905	0.23732
<b><math>rp_2</math>, Euler angles</b>	63.688	0.0197266	5.6824	8.41622	6233.3	1.36292	0.5235261
<b><math>rp_2</math>, axis angle</b>	73.939	0.0197274	5.68251	8.41609	6233.11	1.36292	0.5241948
<b><math>rp_2</math>, quaternion</b>	153.515	0.0198761	5.70398	8.41867	6236.93	1.3629	0.5233601

**Table 3** Comparison of methods using the error metrics described in Section 3.2 for Dataset 2.

Method	Time (s)	$e_{R1}$	$e_{R2}$ (degrees)	$e_t$ (mm)	$e_C$	$rrmse$ (pixels)	$rac$ (mm)
Zhuang [18]	0.014	0.0000625721	0.288076	1.307	47.8309	11.8458	52.65020
Dornaika [3]: Closed Form	0.003	0.404248	24.1399	79.3305	176214	2959.58	5580067.998
Dornaika [3]: Iterative	1.206	1.30484	45.2478	74.8997	157080	1329.87	173943689.69
Hirsh [4]	0.35	0.0000199547	0.149794	0.888279	22.0931	4.66805	2.500515
Li [6]: Dual Quaternion	0.07	0.0000251894	0.185176	0.75443	15.9366	5.24936	14.9587
Li [6]: Kronecker product	0.0001	0.0000227466	0.169176	0.972035	26.4559	5.67147	23.201702
Shah [10]	0.0001	0.0000199547	0.149793	0.834843	19.515	4.6186	2.387767
<b><math>c_1</math>, Euler angles, simultaneous</b>	0.239	0.0000220172	0.164733	0.736446	15.1859	4.35244	5.125558
<b><math>c_1</math>, axis angle, simultaneous</b>	0.14	0.0000220365	0.164714	0.736446	15.1859	4.34548	4.963828
<b><math>c_1</math>, quaternion, simultaneous</b>	0.149	0.0000333404	0.196254	0.736446	15.1859	7.43213	15.024401
<b><math>c_2</math>, Euler angles, simultaneous</b>	0.199	0.000022573	0.168609	0.800019	17.9209	3.96036	0.0863250
<b><math>c_2</math>, axis angle, simultaneous</b>	0.14	0.0000227808	0.171629	0.804379	18.1168	3.96272	0.095928
<b><math>c_2</math>, quaternion, simultaneous</b>	0.181	0.000022573	0.168604	0.800019	17.9209	3.96047	0.086529
<b><math>c_1</math>, Euler angles, separable</b>	0.502	0.0000199547	0.149794	0.834828	19.5143	4.61824	2.38108
<b><math>c_1</math>, axis angle, separable</b>	0.323	0.0000199547	0.149794	0.834836	19.5146	4.61825	2.38061
<b><math>c_1</math>, quaternion, separable</b>	0.689	0.0000199547	0.149795	0.834902	19.5177	4.61847	2.37722
<b><math>c_2</math>, Euler angles, separable</b>	0.301	0.0000199547	0.149793	0.84598	20.0391	4.48836	0.069070
<b><math>c_2</math>, axis angle, separable</b>	0.28	0.0000199547	0.149795	0.845938	20.0371	4.48847	0.069380
<b><math>c_2</math>, quaternion, separable</b>	0.325	0.0000199547	0.149794	0.84595	20.0377	4.48849	0.069498
<b><math>rp_1</math>, Euler angles</b>	5.789	0.0000331533	0.184911	1.00207	28.1162	3.74123	0.0295049
<b><math>rp_1</math>, axis angle</b>	6.189	0.0000331533	0.184911	1.00207	28.1162	3.74123	0.0295049
<b><math>rp_1</math>, quaternion</b>	6.22	0.0000331533	0.184911	1.00207	28.1162	3.74123	0.0295049
<b><math>rp_2</math>, Euler angles</b>	66.702	0.00296179	2.1996	6.31123	1115.29	3.18114	0.44990
<b><math>rp_2</math>, axis angle</b>	48.242	0.00276524	2.12493	6.11936	1048.51	3.1713	0.44034
<b><math>rp_2</math>, quaternion</b>	69.996	0.00295924	2.19865	6.31096	1115.19	3.18101	0.46199

**Table 4** Comparison of methods using the error metrics described in Section 3.2 for Dataset 3.

Method	Time (s)	$e_{R1}$	$e_{R2}$ (degrees)	$e_t$ (mm)	$e_C$	$rrmse$ (pixels)	$rae$ (mm)
Zhuang [18]	0.013	0.765909	35.737	84.21	255288	1752.74	$1.08832 \times 10^8$
Dornaika [3]: Closed Form	0.005	0.0760832	8.90491	97.4986	342216	1512.71	$8.28684 \times 10^{16}$
Dornaika [3]: Iterative	3.083	7.01367	139.069	75.6174	205854	1179.24	$1.66168 \times 10^7$
Hirsh [4]	3.281	0.000146461	0.400659	6.17446	1372.46	39.071	3729.96
Li [6]: Dual Quaternion	0.125	0.000229668	0.55199	5.34571	1028.76	20.7324	1896.01
Li [6]: Kronecker product	0.002	0.000152553	0.42043	4.82104	836.727	31.7476	1832.47
Shah [10]	0.0001	0.000146461	0.400666	2.76823	275.872	9.10238	123.061
$c_1$ , Euler angles, simultaneous	0.472	0.000151291	0.416122	2.652	253.191	7.58227	144.659
$c_1$ , axis angle, simultaneous	0.225	0.000151289	0.416115	2.652	253.191	7.58583	144.482
$c_1$ , quaternion, simultaneous	0.195	0.00015248	0.426517	2.652	253.191	7.83721	143.142
$c_2$ , Euler angles, simultaneous	0.256	0.000153451	0.425433	2.8537	293.17	3.55362	1.92736
$c_2$ , axis angle, simultaneous	0.221	0.000153445	0.424749	2.85365	293.16	3.5553	1.96219
$c_2$ , quaternion, simultaneous	0.187	0.000153914	0.42986	2.85616	293.676	3.5587	1.74438
$c_1$ , Euler angles, separable	0.843	0.000146461	0.400655	2.76854	275.933	9.11944	123.812
$c_1$ , axis angle, separable	0.504	0.000146461	0.400679	2.76841	275.908	9.11817	123.833
$c_1$ , quaternion, separable	1.293	0.000146461	0.400658	2.76854	275.933	9.11947	123.798
$c_2$ , Euler angles, separable	0.458	0.000146461	0.400658	2.85224	292.871	7.37805	1.5171
$c_2$ , axis angle, separable	0.447	0.000146461	0.400658	2.85223	292.869	7.37791	1.51745
$c_2$ , quaternion, separable	0.506	0.000146461	0.400658	2.85222	292.866	7.3776	1.51769
$rp_1$ , Euler angles	10.706	0.000158848	0.433885	2.92055	307.066	2.89018	1.45425
$rp_1$ , axis angle	9.917	0.000158848	0.433885	2.92055	307.066	2.89018	1.45426
$rp_1$ , quaternion	10.521	0.000158848	0.433885	2.92055	307.066	2.89018	1.45426
$rp_2$ , Euler angles	46.056	0.000900894	1.17365	3.12839	352.326	2.67963	1.5875
$rp_2$ , axis angle	49.188	0.000900894	1.17365	3.12839	352.326	2.67963	1.5875
$rp_2$ , quaternion	87.846	0.000900897	1.17365	3.12839	352.327	2.67963	1.58896

**Table 5** Comparison of methods using the error metrics described in Section 3.2 for Dataset 4.

Method	Time (s)	$e_{R1}$	$e_{R2}$ (degrees)	$e_t$ (mm)	$e_C$	$rrmse$ (pixels)	$rae$ (mm)
Zhuang [18]	0.003	0.00775597	2.41835	92.201	170021	288.166	36039.5
Dornaika [3]: Closed Form	0.003	0.010101	2.57979	122.624	300733	420.053	659311
Dornaika [3]: Iterative	1.692	7.97719	173.278	8.05142	1304.49	1235	$1.11892 \times 10^{17}$
Hirsh [4]	3.409	0.000954823	0.350316	6.06421	735.493	6.22611	76.2172
Li [6]: Dual Quaternion	0.018	0.0675828	10.5063	63.6596	81050.9	189.191	232276
Li [6]: Kronecker product	0.001	0.000120951	0.415269	7.2863	1061.8	21.69	4198.79
Shah [10]	0.0001	0.000954823	0.350316	3.12994	195.931	2.27361	22.7013
$c_1$ , Euler angles, simultaneous	0.195	0.000124344	0.422193	3.01615	181.943	2.85969	9.30925
$c_1$ , axis angle, simultaneous	0.129	0.000124321	0.42244	3.01615	181.943	2.85827	9.15721
$c_1$ , quaternion, simultaneous	0.111	0.000124662	0.422864	3.01615	181.943	2.95739	9.59481
$c_2$ , Euler angles, simultaneous	0.142	0.000973168	0.35385	3.12497	195.309	2.38787	1.7146
$c_2$ , axis angle, simultaneous	0.12	0.0009721	0.353469	3.12309	195.073	2.38756	1.72392
$c_2$ , quaternion, simultaneous	0.107	0.000973516	0.354033	3.12428	195.222	2.38988	1.72006
$c_1$ , Euler angles, separable	0.531	0.000954823	0.350316	3.13017	195.959	2.27045	22.7467
$c_1$ , axis angle, separable	0.429	0.000954823	0.350316	3.13001	195.939	2.27319	22.7232
$c_1$ , quaternion, separable	0.843	0.000954824	0.35032	3.13012	195.953	2.27069	22.7303
$c_2$ , Euler angles, separable	0.255	0.000954823	0.350316	3.15556	199.151	1.83788	2.11546
$c_2$ , axis angle, separable	0.255	0.000954823	0.350316	3.15555	199.151	1.8379	2.1149
$c_2$ , quaternion, separable	0.313	0.000954823	0.350316	3.15555	199.151	1.83791	2.11489
$rp_1$ , Euler angles	6.454	0.000103036	0.367112	3.33431	222.352	1.60321	1.43699
$rp_1$ , axis angle	6.843	0.000103036	0.367112	3.33431	222.352	1.60321	1.43699
$rp_1$ , quaternion	11.683	0.000103036	0.367113	3.3343	222.351	1.60321	1.43714
$rp_2$ , Euler angles	18.414	0.000743268	1.08192	4.22232	356.561	1.50483	1.48145
$rp_2$ , axis angle	22.174	0.000743268	1.08192	4.22232	356.561	1.50483	1.48145
$rp_2$ , quaternion	46.835	0.00074373	1.08227	4.22268	356.622	1.50549	1.48562

**Table 6** Comparison of methods using the error metrics described in Section 3.2 for Dataset 5.

Method	Time (s)	$e_{R1}$	$e_{R2}$ (degrees)	$e_t$ (mm)	$e_C$	$rrmse$ (pixels)	$rae$ (mm)
Zhuang [18]	0.004	0.0118914	3.61164	113.639	180792	1190	862073
Dornaika [3]: Closed Form	0.002	0.0505229	7.58041	58.6203	48108.8	211.081	150077
Dornaika [3]: Iterative	1.116	4.36192	95.1924	31.289	13710.4	1206	$1.36857 \times 10^{10}$
Hirsh [4]	0.354	0.000261473	0.199554	152.636	326170	238.041	$1.01182 \times 10^{11}$
Li [6]: Dual Quaternion	0.008	0.010287	4.05685	85.8321	103140	65.5218	62885.7
Li [6]: Kronecker product	0.001	0.000285929	0.203356	4.84945	329.24	7.16294	236.416
Shah [10]	0.0001	0.000261584	0.199265	210.092	617943	439.512	$2.12246 \times 10^{17}$
$c_1$ , Euler angles, simultaneous	0.085	0.0000338659	0.226466	1.28684	23.1834	3.88777	31.421
$c_1$ , axis angle, simultaneous	0.093	0.000287485	0.206804	1.28684	23.1833	3.32417	17.362
$c_1$ , quaternion, simultaneous	0.08	0.0000313139	0.203908	1.28684	23.1834	3.47606	20.3247
$c_2$ , Euler angles, simultaneous	0.089	0.000285658	0.210174	1.99459	55.6977	1.0838	16.4967
$c_2$ , axis angle, simultaneous	0.092	0.000265726	0.202214	1.93993	52.6869	1.05499	13.9331
$c_2$ , quaternion, simultaneous	0.095	0.000265728	0.202212	1.93994	52.6872	1.05499	13.9361
$c_1$ , Euler angles, separable	0.25	0.000261473	0.199555	68.3986	65497.1	97.0019	180519
$c_1$ , axis angle, separable	0.265	0.000261473	0.19954	58.444	47819.8	81.2711	125430
$c_1$ , quaternion, separable	0.362	0.000261473	0.199555	34.2755	16447.3	47.188	33338.9
$c_2$ , Euler angles, separable	0.154	0.000261473	0.199546	83.4457	97484.7	80.4444	124079
$c_2$ , axis angle, separable	0.159	0.000261473	0.199555	56.1978	44214.7	48.1819	35443.8
$c_2$ , quaternion, separable	0.173	0.000261473	0.199555	56.4971	44687	48.4882	36033.6
$rp_1$ , Euler angles	3.445	0.000112519	0.393463	4.43837	275.788	0.648684	1.21898
$rp_1$ , axis angle	3.158	0.000112519	0.393463	4.43836	275.787	0.648684	1.21894
$rp_1$ , quaternion	4.593	0.000112517	0.393459	4.43833	275.783	0.648684	1.21906
$rp_2$ , Euler angles	22.517	0.000647345	1.02564	9.02427	1140.13	0.605089	0.933008
$rp_2$ , axis angle	19.253	0.00064732	1.02562	9.02516	1140.35	0.605088	0.928356
$rp_2$ , quaternion	32.277	0.000643362	1.02226	7.30616	747.319	0.605207	0.955197

**Table 7** Comparison of methods using the error metrics described in Section 3.2 for Dataset 6.  $rrmse$  is computed for each camera.

Method	Time (s)	$e_{R1}$	$e_{R2}$ (degrees)	$e_t$ (mm)	$e_C$	$rrmse_0$ (pixels)	$rrmse_1$ (pixels)	$rae$ (mm)
$c_1$ , Euler angles, simultaneous	0.386	0.000257326	0.193937	1.24552	21.0586	2.31762	2.00706	16.6109
$c_1$ , axis angle, simultaneous	0.407	0.000257326	0.193936	1.24552	21.0586	2.31762	2.00706	16.6109
$c_1$ , quaternion, simultaneous	0.424	0.000257326	0.193936	1.24552	21.0586	2.31762	2.00706	16.6109
$c_2$ , Euler angles, simultaneous	0.242	0.000280977	0.206962	1.9874	53.4269	0.766459	0.774432	15.6238
$c_2$ , axis angle, simultaneous	0.248	0.000249891	0.193788	1.90496	49.1943	0.750998	0.734177	12.6656
$c_2$ , quaternion, simultaneous	0.262	0.00024989	0.193789	1.90496	49.194	0.750993	0.734177	12.6686
$c_1$ , Euler angles, separable	0.708	0.000234965	0.186335	67.016	60837.1	68.7115	62.0413	141154
$c_1$ , axis angle, separable	0.823	0.000234965	0.186335	57.4164	44653.1	57.634	52.0727	100740
$c_1$ , quaternion, separable	1.043	0.000234965	0.186335	33.8565	15522.1	33.5017	30.1025	27709.6
$c_2$ , Euler angles, separable	0.428	0.000234965	0.186322	81.9702	91006.5	57.0089	51.6298	101915
$c_2$ , axis angle, separable	0.46	0.000234965	0.186335	55.2702	41375.6	34.1357	30.7028	29771.8
$c_2$ , quaternion, separable	0.474	0.000234965	0.186335	55.4786	41688.2	34.2896	30.8437	30120.1
$rp_1$ , Euler angles	9.117	0.000114934	0.401383	4.58804	284.219	0.461123	0.470814	1.49774
$rp_1$ , axis angle	9.785	0.000114934	0.401383	4.58803	284.218	0.461123	0.470814	1.49768
$rp_1$ , quaternion	16.697	0.000114932	0.401379	4.588	284.214	0.461122	0.470813	1.49852
$rp_2$ , Euler angles	83.205	0.000583753	0.973613	9.75874	1296.52	0.430003	0.435863	1.22988
$rp_2$ , axis angle	89.531	0.000583745	0.973605	9.75883	1296.54	0.430003	0.435863	1.2324
$rp_2$ , quaternion	88.379	0.00069386	1.06199	10.71	1551.12	0.429859	0.44217	1.25663

minimization problems using three different rotation representations. Our collection of methods was evaluated relative to existing robot-world hand-eye calibration methods.

This collection of methods was extended to be used to calibrate multiple cameras mounted on one robot, and this was demonstrated on datasets with one to three cameras. To the best of our knowledge, there are currently no other robot-world hand-eye calibration methods for multiple cameras, and consequently we believe this work is the first attempt to solve such a problem. We also

introduced a metric, called Reconstruction Accuracy Error, or  $rae$ , to assess a particular method's suitability to reconstruction problems.

Our collections of methods, particularly the  $c_2$  simultaneous method from the first class and both methods in the second class perform consistently well with respect to reconstruction accuracy error, generating  $rae \leq 2$ mm, which is the average distance between a calibration pattern point and the point generated with the robot-world, hand-eye calibration information. This value of  $rae \leq 2$ mm resulted from evaluating the collection of

**Table 8** Comparison of methods using the error metrics described in Section 3.2 for Dataset 7. *rrmse* is computed for each camera.

Method	Time (s)	$e_{R1}$	$e_{R2}$ (degrees)	$e_t$ (mm)	$e_C$	<i>rrmse</i> <sub>0</sub> (pixels)	<i>rrmse</i> <sub>1</sub> (pixels)	<i>rrmse</i> <sub>2</sub> (pixels)	<i>rae</i> (mm)
$c_1$ , Euler angles, simultaneous	1.548	0.000037808	0.223619	1.01891	37.8961	1.70065	1.70483	2.05211	25.5861
$c_1$ , axis angle, simultaneous	1.349	0.0000344302	0.216382	1.01891	37.8961	1.76765	1.86726	1.57613	27.7002
$c_1$ , quaternion, simultaneous	1.13	0.00003705	0.219817	1.01891	37.8961	1.59012	1.59645	1.89843	21.5528
$c_2$ , Euler angles, simultaneous	1.273	0.0000380638	0.234888	1.3724	68.5225	0.777057	0.689395	0.464227	9.86823
$c_2$ , axis angle, simultaneous	1.32	0.0000340799	0.214434	1.32509	63.8607	0.740757	0.672692	0.464665	7.11799
$c_2$ , quaternion, simultaneous	1.656	0.0000340798	0.214439	1.32509	63.8605	0.740759	0.672692	0.464664	7.12014
$c_1$ , Euler angles, separable	3.31	0.0000255085	0.18337	1.11447	45.1969	1.63226	1.62237	0.928388	14.4895
$c_1$ , axis angle, separable	3.18	0.0000255086	0.183363	1.11471	45.2157	1.63213	1.62221	0.928315	14.4774
$c_1$ , quaternion, separable	6.124	0.0000255086	0.183362	1.11481	45.224	1.63209	1.62216	0.9283	14.4771
$c_2$ , Euler angles, separable	2.506	0.0000255086	0.18335	1.11991	45.6158	1.62662	1.61233	0.924561	9.16612
$c_2$ , axis angle, separable	2.669	0.0000255086	0.183363	1.11979	45.6056	1.62658	1.61229	0.924541	9.16691
$c_2$ , quaternion, separable	2.578	0.0000255086	0.183363	1.11979	45.6061	1.62659	1.6123	0.92455	9.16742
$rp_1$ , Euler angles	55.371	0.000106375	0.383085	2.72123	281.057	0.56	0.562183	0.414597	1.12422
$rp_1$ , axis angle	61.656	0.000106375	0.383085	2.72123	281.057	0.56	0.562183	0.414597	1.12423
$rp_1$ , quaternion	67.778	0.000106363	0.38307	2.72111	281.024	0.559993	0.562184	0.414596	1.12366
$rp_2$ , Euler angles	299.438	0.000449848	0.845571	6.79131	1753	0.536306	0.524921	0.393133	1.17076
$rp_2$ , axis angle	359.832	0.000449848	0.845571	6.79131	1753	0.536306	0.524921	0.393133	1.17062
$rp_2$ , quaternion	503.785	0.000450395	0.845975	6.7963	1756.08	0.536307	0.524912	0.393125	1.17389

**Table 9** Comparison of methods using the error metrics described in Section 3.2 for Dataset 8. *rrmse* is computed for each camera.

Method	Time (s)	$e_{R1}$	$e_{R2}$ (degrees)	$e_t$ (mm)	$e_C$	<i>rrmse</i> <sub>0</sub> (pixels)	<i>rrmse</i> <sub>1</sub> (pixels)	<i>rrmse</i> <sub>2</sub> (pixels)	<i>rae</i> (mm)
$c_1$ , Euler angles, simultaneous	1.372	0.0000332003	0.208999	1.03046	34.7303	2.51556	3.04886	1.38591	35.3555
$c_1$ , axis angle, simultaneous	1.191	0.0000215955	0.172318	1.03046	34.7303	1.47545	1.74632	0.830485	9.76088
$c_1$ , quaternion, simultaneous	0.998	0.0000247851	0.177514	1.03046	34.7303	1.67143	1.81211	0.984151	10.5367
$c_2$ , Euler angles, simultaneous	1.114	0.0000330719	0.221522	1.42353	65.1598	0.805084	0.885025	0.429181	3.74888
$c_2$ , axis angle, simultaneous	1.164	0.0000288111	0.197555	1.36356	60.1969	0.776654	0.861649	0.422205	2.18689
$c_2$ , quaternion, simultaneous	1.452	0.0000288111	0.197561	1.36355	60.1956	0.776668	0.861652	0.422208	2.18551
$c_1$ , Euler angles, separable	2.792	0.0000189285	0.157639	1.10155	39.413	1.82487	1.83353	0.954764	9.52457
$c_1$ , axis angle, separable	2.878	0.0000189285	0.157637	1.10165	39.4201	1.82476	1.83337	0.954722	9.50306
$c_1$ , quaternion, separable	4.815	0.0000189285	0.157637	1.10166	39.4209	1.82475	1.83337	0.954719	9.50292
$c_2$ , Euler angles, separable	2.241	0.0000189285	0.157627	1.10651	39.7034	1.82112	1.81528	0.952705	4.28782
$c_2$ , axis angle, separable	2.33	0.0000189285	0.157637	1.10644	39.6979	1.8211	1.81525	0.952688	4.28961
$c_2$ , quaternion, separable	2.457	0.0000189285	0.157637	1.10644	39.6982	1.8211	1.81526	0.952697	4.28607
$rp_1$ , Euler angles	44.95	0.0000769972	0.336918	2.50928	203.51	0.667398	0.745895	0.381425	0.901561
$rp_1$ , axis angle	47.474	0.0000769971	0.336919	2.50928	203.509	0.667398	0.745895	0.381425	0.901595
$rp_1$ , quaternion	47.888	0.0000769964	0.336917	2.50927	203.509	0.667399	0.745895	0.381425	0.901831
$rp_2$ , Euler angles	249.902	0.000611282	0.980505	6.85716	1591.65	0.651493	0.722737	0.361992	1.00248
$rp_2$ , axis angle	264.648	0.000611284	0.980507	6.85717	1591.66	0.651493	0.722737	0.361992	1.00167
$rp_2$ , quaternion	267.476	0.000612111	0.981022	6.84548	1585.09	0.651488	0.722743	0.361669	1.01235

methods on a range of real datasets representing different mounting configurations and robot positions relative to the world coordinate frame.

**Acknowledgements** We also would like to thank anonymous reviewers of our previous paper [15] and this paper for their helpful comments.

## References

1. Opencv. <http://opencv.org/>. Version 2.4.9
2. Agarwal, S., Mierle, K., Others: Ceres solver. <http://ceres-solver.org>
3. Dornaika, F., Horaud, R.: Simultaneous robot-world and hand-eye calibration. *Robotics and Automation, IEEE Transactions on* **14**(4), 617–622 (1998)
4. Hirsh, R.L., DeSouza, G.N., Kak, A.C.: An iterative approach to the hand-eye and base-world calibration problem. In: *Robotics and Automation, 2001. Proceedings 2001 ICRA. IEEE International Conference on*, vol. 3, pp. 2171–2176. IEEE (2001)
5. Horaud, R., Dornaika, F.: Hand-eye calibration. *The international journal of robotics research* **14**(3), 195–210 (1995)
6. Li, A., Lin, W., Defeng, W.: Simultaneous robot-world and hand-eye calibration using dual-quaternions and kronecker product. *International Journal of Physical Sciences* **5**(10), 1530–1536 (2010)
7. Lourakis, M.: levmar: Levenberg-marquardt nonlinear least squares algorithms in C/C++. [web page] <http://www.ics.forth.gr/~lourakis/levmar/> (Jul. 2004). [Accessed on 18 Nov. 2014.]
8. Malti, A.: Hand-eye calibration with epipolar constraints: Application to endoscopy. *Robotics and Autonomous Systems* **61**(2), 161–169 (2013)
9. Marquardt, D.W.: An algorithm for least-squares estimation of nonlinear parameters. *Journal of the Society for Industrial & Applied Mathematics* **11**(2), 431–441 (1963)



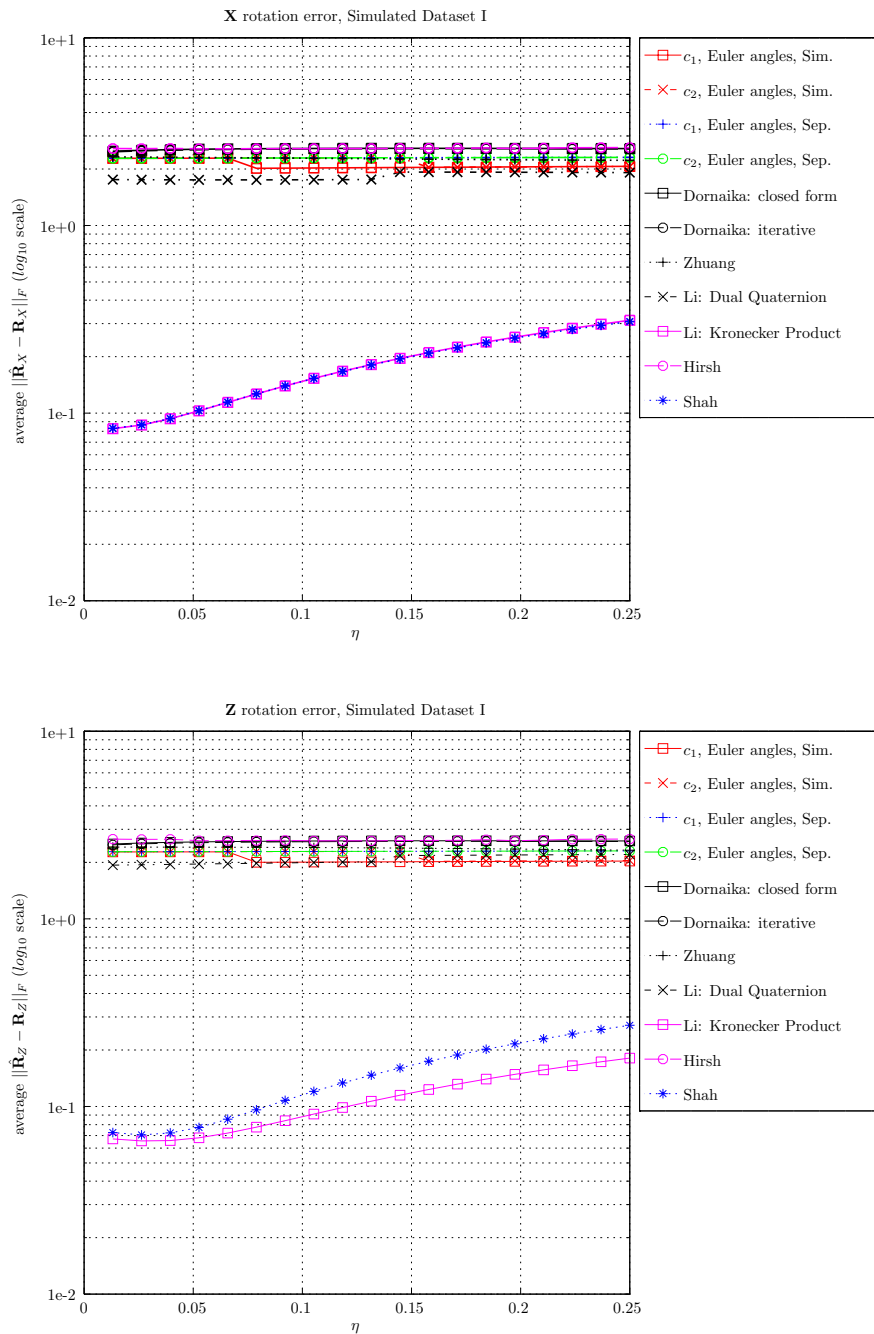


**Fig. 4 Best viewed in color.** Rotation error results for Simulated Dataset I, as compared to the ground truth  $\mathbf{X}$  and  $\mathbf{Z}$ , using the four metrics of Subsection 4.1.

10. Shah, M.: Solving the robot-world/hand-eye calibration problem using the kronecker product. *ASME Journal of Mechanisms and Robotics* **5**(3), 031,007–031,007–7 (2013)
11. Shiu, Y.C., Ahmad, S.: Calibration of wrist-mounted robotic sensors by solving homogeneous transform equations of the form  $\mathbf{ax}=\mathbf{xb}$ . *Robotics and Automation, IEEE Transactions on* **5**(1), 16–29 (1989)
12. Strobl, K.H., Hirzinger, G.: Optimal hand-eye calibration. In: 2006 IEEE/RSJ International Conference on Intelligent Robots and Systems, pp. 4647–4653 (2006). DOI 10.1109/IROS.2006.2822250
13. Tabb, A.: Shape from silhouette probability maps: reconstruction of thin objects in the presence of silhouette extraction and calibration error. In: *Computer Vision and Pattern Recognition (CVPR), 2013 IEEE Conference on* (2013)
14. Tabb, A.: Data from: Solving the robot-world hand-eye(s) calibration problem with iterative methods (2017). DOI 10.15482/USDA.ADC/1340592. URL <http://dx.doi.org/10.15482/USDA.ADC/1340592>

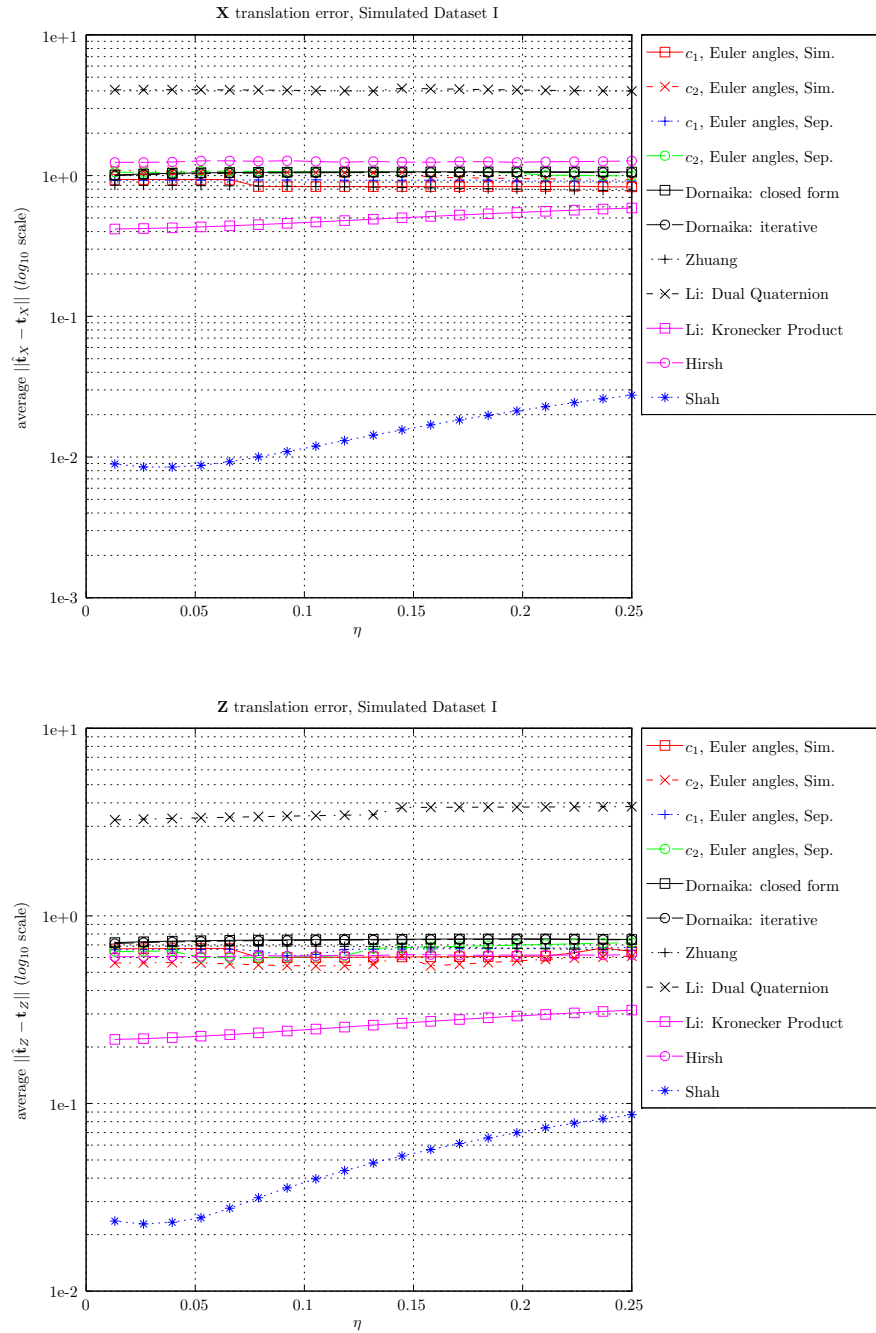


**Fig. 5 Best viewed in color.** Translation error results for Simulated Dataset I, as compared to the ground truth  $\mathbf{X}$  and  $\mathbf{Z}$ , using the four metrics of Subsection 4.1.

- Tabb, A., Ahmad Yousef, K.: Parameterizations for reducing camera reprojection error for robot-world hand-eye calibration. In: IEEE RSJ International Conference on Intelligent Robots and Systems, pp. 3030–3037 (2015)
- Triggs, B., McLauchlan, P.F., Hartley, R.I., Fitzgibbon, A.W.: Bundle adjustment - a modern synthesis. In: Proceedings of the International Workshop on Vision Algorithms: Theory and Practice, ICCV '99, pp. 298–372. Springer-Verlag, London, UK, UK (2000). URL <http://dl.acm.org/citation.cfm?id=646271.685629>
- Zhang, Z.: A flexible new technique for camera calibration. Pattern Analysis and Machine Intelligence, IEEE Transactions on **22**(11), 1330–1334 (2000). DOI 10.1109/34.888718
- Zhuang, H., Roth, Z.S., Sudhakar, R.: Simultaneous robot/world and tool/flange calibration by solving homogeneous transformation equations of the form  $ax=yb$ . Robotics and Automation, IEEE Transactions on **10**(4), 549–554 (1994). DOI 10.1109/70.313105

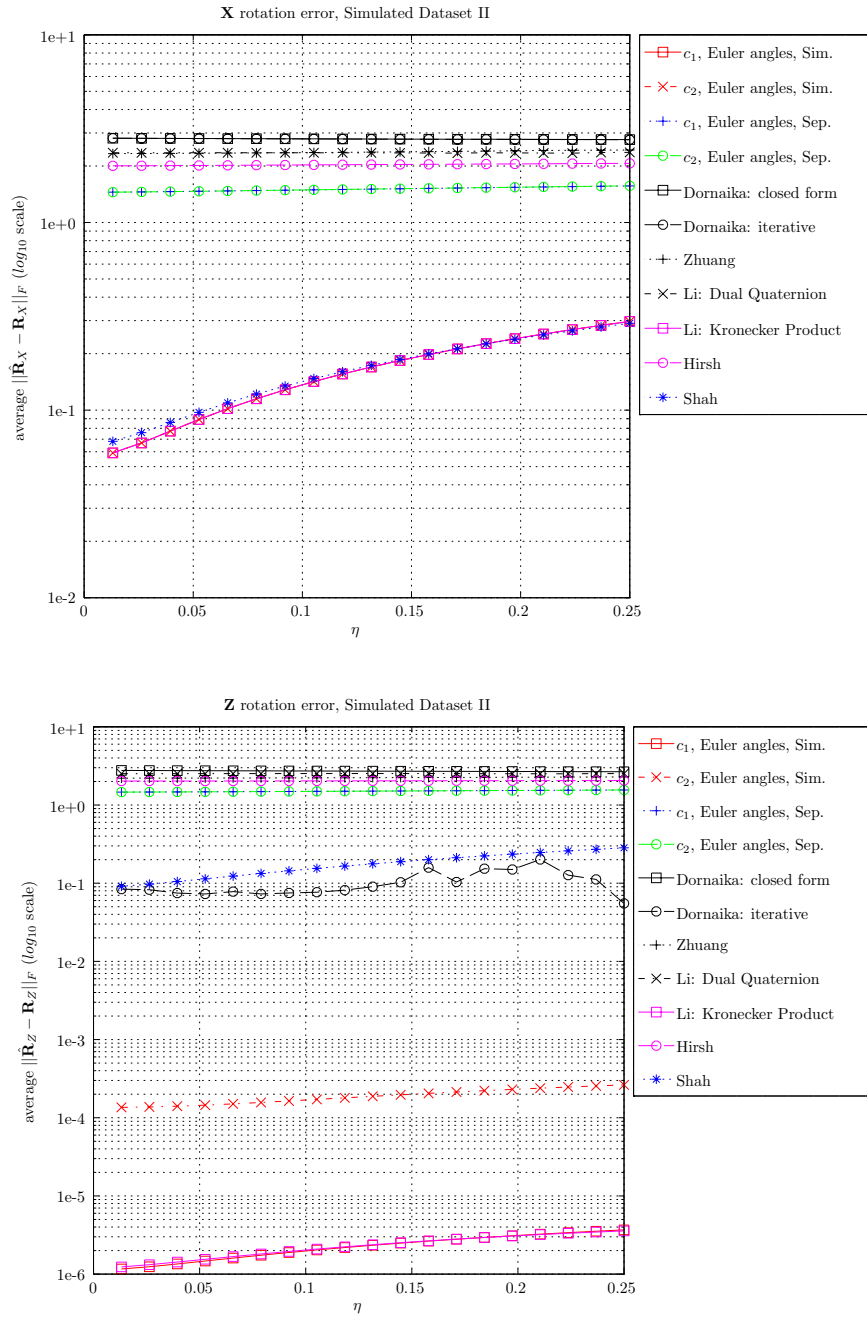


**Fig. 6 Best viewed in color.** Rotation error results for Simulated Dataset II, as compared to the ground truth  $\mathbf{X}$  and  $\mathbf{Z}$ , using the four metrics of Subsection 4.1.

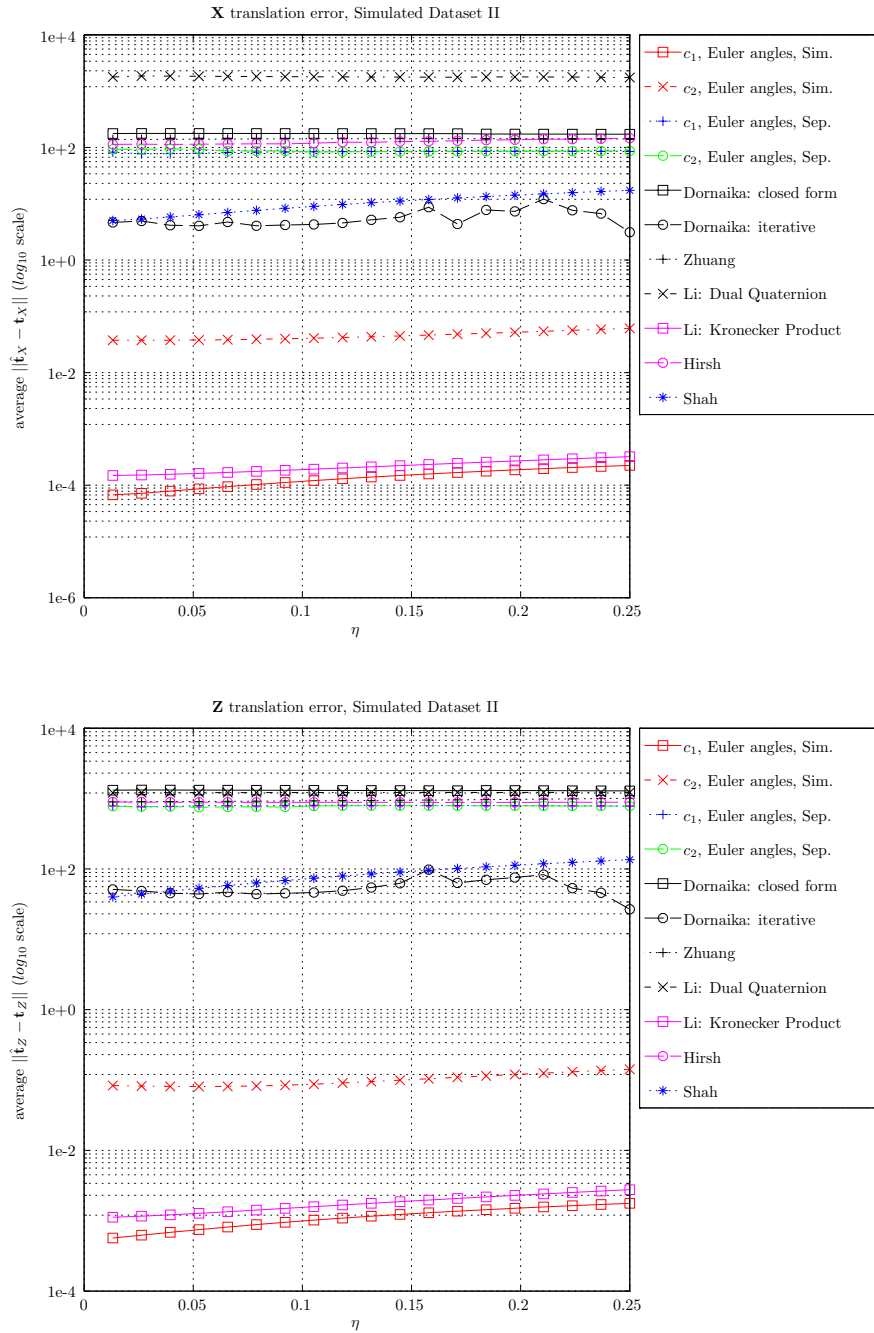


**Fig. 7 Best viewed in color.** Translation error results for Simulated Dataset II, as compared to the ground truth  $\mathbf{X}$  and  $\mathbf{Z}$ , using the four metrics of Subsection 4.1.

## 7 Erratum

We regret that there were some errors in the original paper, concerned mostly with the computation of the mean translation error  $e_t$  (Section 3.2.2, Equation 27).

Specifically,

1. The computation of  $e_t$  was incorrect in our software used to generate the results in tables 2-9 in the original paper.
2. The labeling of units of  $e_t$  was incorrect; it should have been  $\text{mm}^2$ .
3. Tables with corrected results are included in this erratum section, in tables 10-17.
4. The software was released with the paper at [14]; this software has been upgraded to present-day libraries and the error in computing  $e_t$  noted here has been corrected.
5. Since the underlying libraries supporting the software has undergone revision since we prepared the results for the original paper, there are slight differences in the numerical results despite using the same input. Consequently, we included completely refreshed results in tables 10-17.

**Table 10** Erratum: Comparison of methods using the error metrics described in Section 3.2 for Dataset 1.

Method	Time (s)	$e_{R1}$	$e_{R2}$ (degrees)	$e_t$ (mm <sup>2</sup> )	$e_C$	$rrmse$ (pixels)	$rac$ (mm)
Zhuang [18]	0.0210	0.000101	0.33641	233.243	233.243	4.35291	434.01527
Dornaika [3]: Closed Form	0.0050	0.261051	19.51617	330046.750	330047.011	761.54201	158329.92262
Dornaika [3]: Iterative	3.0130	1.947004	58.65204	283023.041	283024.988	272.69726	$2.3137 \times 10^8$
Hirsh [4]	1.847	0.000098	0.33164	359.328	359.328	3.68832	189.53753
Li [6]: Dual Quaternion	0.479	0.000174	0.50621	320.173	320.174	4.30732	103.75765
Li [6]: Kronecker product	0.002	0.000102	0.34782	446.079	446.080	5.41762	388.56442
Shah [10]	0.002	0.000098	0.33164	235.577	235.577	4.10188	403.65687
<b><math>c_1</math>, Euler angles, simultaneous</b>	0.409	0.000268	0.62287	215.364	215.365	12.13016	772.87492
<b><math>c_1</math>, axis angle, simultaneous</b>	0.337	0.000108	0.36440	215.364	215.364	3.62682	267.99188
<b><math>c_1</math>, quaternion, simultaneous</b>	0.408	0.000109	0.36474	215.364	215.364	3.62637	266.80140
<b><math>c_2</math>, Euler angles, simultaneous</b>	0.403	0.000112	0.36726	278.692	278.692	1.67244	5.82028
<b><math>c_2</math>, axis angle, simultaneous</b>	0.423	0.000103	0.35071	262.214	262.214	1.66791	5.01778
<b><math>c_2</math>, quaternion, simultaneous</b>	0.550	0.000103	0.35066	262.213	262.213	1.66771	5.00039
<b><math>c_1</math>, Euler angles, separable</b>	1.277	0.000098	0.33164	235.524	235.524	4.09966	403.09689
<b><math>c_1</math>, axis angle, separable</b>	0.763	0.000098	0.33164	235.572	235.572	4.10052	403.31766
<b><math>c_1</math>, quaternion, separable</b>	1.699	0.000098	0.33164	235.433	235.433	4.09920	403.33220
<b><math>c_2</math>, Euler angles, separable</b>	1.040	0.000098	0.33164	269.760	269.760	2.29070	5.64531
<b><math>c_2</math>, axis angle, separable</b>	0.777	0.000098	0.33164	269.744	269.744	2.29092	5.64409
<b><math>c_2</math>, quaternion, separable</b>	0.801	0.000098	0.33164	269.805	269.806	2.29094	5.65983
<b><math>rp_1</math>, Euler angles</b>	14.260	0.000128	0.38464	338.783	338.784	1.56908	0.23804
<b><math>rp_1</math>, axis angle</b>	15.072	0.000128	0.38449	338.666	338.666	1.56908	0.23743
<b><math>rp_1</math>, quaternion</b>	15.212	0.000128	0.38449	338.666	338.666	1.56908	0.23743
<b><math>rp_2</math>, Euler angles</b>	63.0020	0.019727	5.68253	6233.290	6233.309	1.36298	0.52385
<b><math>rp_2</math>, axis angle</b>	72.797	0.019728	5.68265	6233.127	6233.147	1.36298	0.52243
<b><math>rp_2</math>, quaternion</b>	149.636	0.019878	5.70424	6237.134	6237.154	1.36296	0.52574

**Table 11** Erratum: Comparison of methods using the error metrics described in Section 3.2 for Dataset 2.

Method	Time (s)	$e_{R1}$	$e_{R2}$ (degrees)	$e_t$ (mm <sup>2</sup> )	$e_C$	$rrmse$ (pixels)	$rae$ (mm)
Zhuang [18]	0.014	0.000063	0.28809	47.827	47.827	11.84704	52.66809
Dornaika [3]: Closed Form	0.003	0.404248	24.13993	176213.072	176213.476	2960.45045	$5.580249 \times 10^6$
Dornaika [3]: Iterative	1.056	1.304833	45.24779	157078.853	157080.158	1329.87157	$1.7394 \times 10^8$
Hirsh [4]	0.353	0.000020	0.14979	22.096	22.096	4.66845	2.50364
Li [6]: Dual Quaternion	0.098	0.000025	0.18517	15.937	15.937	5.24925	14.96466
Li [6]: Kronecker product	0.001	0.000023	0.16918	26.456	26.456	5.67126	23.21517
Shah [10]	0.001	0.000020	0.14979	19.516	19.516	4.61892	2.38927
<b><math>c_1</math>, Euler angles, simultaneous</b>	0.237	0.000022	0.16473	15.187	15.187	4.35282	5.13016
<b><math>c_1</math>, axis angle, simultaneous</b>	0.114	0.000022	0.16471	15.187	15.187	4.34575	4.96597
<b><math>c_1</math>, quaternion, simultaneous</b>	0.117	0.000033	0.19625	15.187	15.187	7.43073	15.01492
<b><math>c_2</math>, Euler angles, simultaneous</b>	0.159	0.000023	0.16861	17.922	17.922	3.96063	0.08592
<b><math>c_2</math>, axis angle, simultaneous</b>	0.111	0.000023	0.17163	18.118	18.118	3.96301	0.09631
<b><math>c_2</math>, quaternion, simultaneous</b>	0.145	0.000023	0.16861	17.922	17.922	3.96074	0.08657
<b><math>c_1</math>, Euler angles, separable</b>	0.388	0.000020	0.14979	19.515	19.515	4.61856	2.38316
<b><math>c_1</math>, axis angle, separable</b>	0.247	0.000020	0.14980	19.515	19.515	4.61857	2.38311
<b><math>c_1</math>, quaternion, separable</b>	0.527	0.000020	0.14980	19.518	19.518	4.61879	2.38038
<b><math>c_2</math>, Euler angles, separable</b>	0.293	0.000020	0.14979	20.040	20.040	4.48860	0.06919
<b><math>c_2</math>, axis angle, separable</b>	0.219	0.000020	0.14980	20.038	20.038	4.48871	0.06923
<b><math>c_2</math>, quaternion, separable</b>	0.325	0.000020	0.14979	20.039	20.039	4.48872	0.06924
<b><math>rp_1</math>, Euler angles</b>	5.850	0.000033	0.18490	28.106	28.106	3.74137	0.02943
<b><math>rp_1</math>, axis angle</b>	5.749	0.000033	0.18490	28.106	28.106	3.74137	0.02943
<b><math>rp_1</math>, quaternion</b>	5.812	0.000033	0.18490	28.106	28.106	3.74137	0.02943
<b><math>rp_2</math>, Euler angles</b>	61.095	0.002584	2.05375	1003.534	1003.537	3.17178	0.42202
<b><math>rp_2</math>, axis angle</b>	45.762	0.002960	2.19890	1114.867	1114.870	3.18069	0.45105
<b><math>rp_2</math>, quaternion</b>	54.227	0.002814	2.14382	1077.202	1077.204	3.20080	0.48394

**Table 12** Erratum: Comparison of methods using the error metrics described in Section 3.2 for Dataset 3.

Method	Time (s)	$e_{R1}$	$e_{R2}$ (degrees)	$e_t$ (mm <sup>2</sup> )	$e_C$	$rrmse$ (pixels)	$rae$ (mm)
Zhuang [18]	0.012	0.748187	35.29844	255631.854	255632.602	1738.74388	$1.1469 \times 10^8$
Dornaika [3]: Closed Form	0.001	0.076083	8.90484	342216.217	342216.293	1512.72147	$8.2868 \times 10^{16}$
Dornaika [3]: Iterative	3.027	6.573935	130.42109	242775.069	242781.643	1082.19641	$7.5994 \times 10^{11}$
Hirsh [4]	2.824	0.000146	0.40067	1372.050	1372.050	39.06440	3728.99175
Li [6]: Dual Quaternion	0.132	0.000229	0.55140	1029.034	1029.035	20.73318	1897.51411
Li [6]: Kronecker product	0.002	0.000153	0.42043	836.723	836.723	31.74729	1832.37089
Shah [10]	0.001	0.000146	0.40067	275.867	275.867	9.10223	123.07597
$c_1$ , Euler angles, simultaneous	0.368	0.000151	0.41612	253.188	253.189	7.58226	144.67042
$c_1$ , axis angle, simultaneous	0.179	0.000151	0.41611	253.188	253.189	7.58582	144.49466
$c_1$ , quaternion, simultaneous	0.188	0.000152	0.42652	253.188	253.189	7.83734	143.14568
$c_2$ , Euler angles, simultaneous	0.200	0.000153	0.42543	293.168	293.169	3.55318	1.92455
$c_2$ , axis angle, simultaneous	0.222	0.000153	0.42475	293.158	293.158	3.55486	1.96232
$c_2$ , quaternion, simultaneous	0.145	0.000154	0.42986	293.674	293.674	3.55825	1.74497
$c_1$ , Euler angles, separable	0.692	0.000146	0.40066	275.928	275.928	9.11933	123.84680
$c_1$ , axis angle, separable	0.496	0.000146	0.40068	275.903	275.903	9.11806	123.85266
$c_1$ , quaternion, separable	1.007	0.000146	0.40066	275.927	275.928	9.11936	123.82410
$c_2$ , Euler angles, separable	0.367	0.000146	0.40066	292.867	292.867	7.37767	1.51762
$c_2$ , axis angle, separable	0.433	0.000146	0.40066	292.865	292.865	7.37754	1.51853
$c_2$ , quaternion, separable	0.400	0.000146	0.40066	292.862	292.863	7.37722	1.51869
$rp_1$ , Euler angles	10.689	0.000159	0.43389	307.060	307.060	2.88994	1.45434
$rp_1$ , axis angle	9.901	0.000159	0.43389	307.060	307.060	2.88994	1.45434
$rp_1$ , quaternion	11.359	0.000159	0.43389	307.060	307.060	2.88994	1.45434
$rp_2$ , Euler angles	56.981	0.000901	1.17360	352.352	352.353	2.67935	1.58771
$rp_2$ , axis angle	51.035	0.000901	1.17360	352.352	352.353	2.67935	1.58771
$rp_2$ , quaternion	85.253	0.000901	1.17360	352.353	352.354	2.67935	1.58854

**Table 13** Erratum: Comparison of methods using the error metrics described in Section 3.2 for Dataset 4.

Method	Time (s)	$e_{R1}$	$e_{R2}$ (degrees)	$e_t$ (mm <sup>2</sup> )	$e_C$	$rrmse$ (pixels)	$rae$ (mm)
Zhuang [18]	0.004	0.007756	2.41826	170020.300	170020.307	288.16520	36039.75161
Dornaika [3]: Closed Form	0.002	0.010101	2.57979	300732.854	300732.865	420.05342	659309.84883
Dornaika [3]: Iterative	1.684	7.977799	173.35861	1270.043	1278.021	1247.83275	$1.0814 \times 10^{17}$
Hirsh [4]	2.837	0.000095	0.35031	735.043	735.043	6.22324	76.19298
Li [6]: Dual Quaternion	0.025	0.067583	10.50628	81050.738	81050.806	189.19125	232276.86638
Li [6]: Kronecker product	0.001	0.000121	0.41527	1061.804	1061.804	21.68992	4198.79638
Shah [10]	0.001	0.000095	0.35031	195.932	195.932	2.27370	22.70185
$c_1$ , Euler angles, simultaneous	0.194	0.000124	0.42219	181.943	181.943	2.85971	9.30873
$c_1$ , axis angle, simultaneous	0.128	0.000124	0.42244	181.943	181.943	2.85830	9.15718
$c_1$ , quaternion, simultaneous	0.107	0.000125	0.42286	181.943	181.943	2.95747	9.60132
$c_2$ , Euler angles, simultaneous	0.143	0.000097	0.35385	195.308	195.308	2.38794	1.71308
$c_2$ , axis angle, simultaneous	0.125	0.000097	0.35347	195.072	195.072	2.38763	1.72264
$c_2$ , quaternion, simultaneous	0.103	0.000097	0.35403	195.221	195.221	2.38995	1.72108
$c_1$ , Euler angles, separable	0.479	0.000095	0.35031	195.960	195.960	2.27053	22.74722
$c_1$ , axis angle, separable	0.388	0.000095	0.35031	195.940	195.940	2.27327	22.72429
$c_1$ , quaternion, separable	0.871	0.000095	0.35032	195.953	195.953	2.27077	22.73063
$c_2$ , Euler angles, separable	0.262	0.000095	0.35031	199.151	199.152	1.83791	2.11556
$c_2$ , axis angle, separable	0.252	0.000095	0.35031	199.151	199.151	1.83794	2.11534
$c_2$ , quaternion, separable	0.310	0.000095	0.35031	199.151	199.151	1.83794	2.11532
$rp_1$ , Euler angles	6.199	0.000103	0.36711	222.360	222.360	1.60324	1.43670
$rp_1$ , axis angle	6.833	0.000103	0.36711	222.360	222.360	1.60324	1.43670
$rp_1$ , quaternion	9.080	0.000103	0.36712	222.359	222.359	1.60324	1.43671
$rp_2$ , Euler angles	16.913	0.000744	1.08210	356.566	356.566	1.50485	1.48190
$rp_2$ , axis angle	18.923	0.000744	1.08210	356.566	356.566	1.50485	1.48190
$rp_2$ , quaternion	40.511	0.000744	1.08215	356.526	356.527	1.74254	1.77705

**Table 14** Erratum: Comparison of methods using the error metrics described in Section 3.2 for Dataset 5.

Method	Time (s)	$e_{R1}$	$e_{R2}$ (degrees)	$e_t$ (mm <sup>2</sup> )	$e_C$	$rrmse$ (pixels)	$rae$ (mm)
Zhuang [18]	0.002	0.011891	3.61164	180792.059	180792.071	1189.98270	863192.48952
Dornaika [3]: Closed Form	0.001	0.050523	7.58042	12907.087	12907.138	205.56865	656742.22560
Dornaika [3]: Iterative	0.915	3.793803	87.04476	4479.553	4483.347	1663.75498	$2.4452 \times 10^7$
Hirsh [4]	0.255	0.000026	0.19955	326216.272	326216.272	238.06937	$2.0220 \times 10^{15}$
Li [6]: Dual Quaternion	0.006	0.010035	4.05808	103138.092	103138.102	65.50840	62872.32472
Li [6]: Kronecker product	0.001	0.000029	0.20336	329.240	329.240	7.16277	236.40669
Shah [10]	0.001	0.000026	0.19928	344980.375	344980.375	360.16806	$7.2411 \times 10^{16}$
$c_1$ , Euler angles, simultaneous	0.089	0.000034	0.22647	23.183	23.183	3.88770	31.41986
$c_1$ , axis angle, simultaneous	0.095	0.000029	0.20681	23.183	23.183	3.32425	17.35940
$c_1$ , quaternion, simultaneous	0.076	0.000031	0.20391	23.183	23.183	3.47615	20.36387
$c_2$ , Euler angles, simultaneous	0.087	0.000029	0.21017	55.699	55.699	1.08380	16.49256
$c_2$ , axis angle, simultaneous	0.095	0.000027	0.20221	52.688	52.688	1.05500	13.92408
$c_2$ , quaternion, simultaneous	0.073	0.000027	0.20221	52.689	52.689	1.05500	13.92713
$c_1$ , Euler angles, separable	0.194	0.000026	0.19955	65500.206	65500.206	97.00420	180566.92944
$c_1$ , axis angle, separable	0.208	0.000026	0.19954	47820.619	47820.619	81.27227	125506.43481
$c_1$ , quaternion, separable	0.364	0.000026	0.19956	16447.438	16447.438	47.18953	33340.81463
$c_2$ , Euler angles, separable	0.149	0.000026	0.19955	97722.408	97722.408	80.58572	124624.37003
$c_2$ , axis angle, separable	0.127	0.000026	0.19956	44379.701	44379.701	48.28915	35645.32220
$c_2$ , quaternion, separable	0.129	0.000026	0.19956	45070.128	45070.128	48.73628	36510.79696
$rp_1$ , Euler angles	3.457	0.000113	0.39344	275.759	275.759	0.64876	1.21893
$rp_1$ , axis angle	3.575	0.000113	0.39344	275.758	275.758	0.64876	1.21889
$rp_1$ , quaternion	4.626	0.000113	0.39344	275.754	275.754	0.64876	1.21887
$rp_2$ , Euler angles	20.548	0.000647	1.02519	1115.528	1115.528	0.60515	0.95055
$rp_2$ , axis angle	18.775	0.000647	1.02517	1115.735	1115.736	0.60515	0.95095
$rp_2$ , quaternion	16.906	0.000633	1.01357	780.246	780.247	0.60535	0.95353

**Table 15** Erratum: Comparison of methods using the error metrics described in Section 3.2 for Dataset 6.  $rrmse$  is computed for each camera

Method	Time (s)	$e_{R1}$	$e_{R2}$ (degrees)	$e_t$ (mm <sup>2</sup> )	$e_C$	$rrmse_0$ (pixels)	$rrmse_1$ (pixels)	$rae$ (mm)
$c_1$ , Euler angles, simultaneous	0.379	0.000026	0.19394	21.058	21.058	2.31750	2.00713	16.60861
$c_1$ , axis angle, simultaneous	0.324	0.000026	0.19394	21.058	21.058	2.31750	2.00713	16.60861
$c_1$ , quaternion, simultaneous	0.329	0.000026	0.19394	21.058	21.058	2.31750	2.00713	16.60861
$c_2$ , Euler angles, simultaneous	0.188	0.000028	0.20696	53.429	53.429	0.76638	0.77438	15.62373
$c_2$ , axis angle, simultaneous	0.249	0.000025	0.19379	49.196	49.196	0.75096	0.73416	12.66734
$c_2$ , quaternion, simultaneous	0.258	0.000025	0.19379	49.196	49.196	0.75095	0.73416	12.66495
$c_1$ , Euler angles, separable	0.551	0.000023	0.18634	60839.760	60839.760	68.71189	62.04204	141166.19116
$c_1$ , axis angle, separable	0.629	0.000023	0.18634	44654.582	44654.582	57.63439	52.07320	100711.15406
$c_1$ , quaternion, separable	0.801	0.000023	0.18634	15522.257	15522.257	33.50245	30.10268	27704.61122
$c_2$ , Euler angles, separable	0.335	0.000023	0.18632	91211.109	91211.109	57.10190	51.71440	102266.48506
$c_2$ , axis angle, separable	0.355	0.000023	0.18634	41522.221	41522.222	34.20819	30.76903	29935.04867
$c_2$ , quaternion, separable	0.366	0.000023	0.18634	42030.021	42030.021	34.45783	30.99755	30503.05925
$rp_1$ , Euler angles	8.851	0.000115	0.40124	284.033	284.033	0.46116	0.47084	1.49903
$rp_1$ , axis angle	9.324	0.000115	0.40124	284.032	284.032	0.46116	0.47084	1.49913
$rp_1$ , quaternion	16.287	0.000115	0.40124	284.028	284.028	0.46116	0.47084	1.49854
$rp_2$ , Euler angles	90.490	0.000716	1.07923	1479.389	1479.390	0.42986	0.43418	1.17942
$rp_2$ , axis angle	92.689	0.000716	1.07909	1478.408	1478.408	0.42986	0.43417	1.18624
$rp_2$ , quaternion	109.332	0.000706	1.07121	1546.118	1546.119	0.42975	0.43527	1.22238



**Table 16** Erratum: Comparison of methods using the error metrics described in Section 3.2 for Dataset 7. *rrmse* is computed for each camera

Method	Time (s)	$e_{R1}$	$e_{R2}$ (degrees)	$e_t(\text{mm}^2)$	$e_C$	<i>rrmse</i> <sub>0</sub> (pixels)	<i>rrmse</i> <sub>1</sub> (pixels)	<i>rrmse</i> <sub>2</sub> (pixels)	<i>rae</i> (mm)
$c_1$ , Euler angles, simultaneous	1.239	0.000038	0.22362	37.896	37.896	1.70064	1.70482	2.05210	25.57334
$c_1$ , axis angle, simultaneous	1.074	0.000034	0.21638	37.896	37.896	1.76764	1.86725	1.57616	27.67145
$c_1$ , quaternion, simultaneous	0.940	0.000037	0.21982	37.896	37.896	1.59013	1.59645	1.89845	21.54823
$c_2$ , Euler angles, simultaneous	1.266	0.000038	0.23489	68.522	68.522	0.77711	0.68944	0.46426	9.88793
$c_2$ , axis angle, simultaneous	1.086	0.000034	0.21444	63.860	63.860	0.74081	0.67274	0.46470	7.12096
$c_2$ , quaternion, simultaneous	1.657	0.000034	0.21444	63.860	63.860	0.74081	0.67274	0.46470	7.11958
$c_1$ , Euler angles, separable	2.740	0.000026	0.18337	45.197	45.197	1.63227	1.62238	0.92840	14.48648
$c_1$ , axis angle, separable	2.632	0.000026	0.18336	45.215	45.215	1.63214	1.62222	0.92833	14.47376
$c_1$ , quaternion, separable	5.425	0.000026	0.18336	45.224	45.224	1.63210	1.62217	0.92832	14.47621
$c_2$ , Euler angles, separable	1.973	0.000026	0.18335	45.615	45.615	1.62664	1.61234	0.92458	9.16592
$c_2$ , axis angle, separable	2.278	0.000026	0.18336	45.605	45.605	1.62660	1.61231	0.92456	9.16792
$c_2$ , quaternion, separable	2.539	0.000026	0.18336	45.606	45.606	1.62661	1.61231	0.92457	9.16702
$rp_1$ , Euler angles	50.378	0.000106	0.38311	281.083	281.083	0.56004	0.56222	0.41462	1.12430
$rp_1$ , axis angle	53.302	0.000106	0.38311	281.083	281.083	0.56004	0.56222	0.41462	1.12431
$rp_1$ , quaternion	66.758	0.000106	0.38310	281.050	281.050	0.56003	0.56222	0.41461	1.12354
$rp_2$ , Euler angles	254.175	0.000450	0.84546	1752.721	1752.721	0.53634	0.52495	0.39315	1.15802
$rp_2$ , axis angle	271.251	0.000450	0.84546	1752.721	1752.721	0.53634	0.52495	0.39315	1.15792
$rp_2$ , quaternion	415.247	0.000450	0.84596	1755.846	1755.847	0.53635	0.52495	0.39314	1.17216

**Table 17** Erratum: Comparison of methods using the error metrics described in Section 3.2 for Dataset 8. *rrmse* is computed for each camera

Method	Time (s)	$e_{R1}$	$e_{R2}$ (degrees)	$e_t(\text{mm}^2)$	$e_C$	<i>rrmse</i> <sub>0</sub> (pixels)	<i>rrmse</i> <sub>1</sub> (pixels)	<i>rrmse</i> <sub>2</sub> (pixels)	<i>rae</i> (mm)
$c_1$ , Euler angles, simultaneous	1.380	0.000033	0.20899	34.731	34.731	2.51484	3.04888	1.38608	35.34176
$c_1$ , axis angle, simultaneous	1.163	0.000022	0.17233	34.731	34.731	1.47551	1.74641	0.83057	9.75977
$c_1$ , quaternion, simultaneous	1.000	0.000025	0.17752	34.731	34.731	1.67117	1.81219	0.98439	10.54219
$c_2$ , Euler angles, simultaneous	1.123	0.000033	0.22152	65.159	65.159	0.80521	0.88514	0.42918	3.75085
$c_2$ , axis angle, simultaneous	1.169	0.000029	0.19755	60.197	60.197	0.77679	0.86174	0.42224	2.18616
$c_2$ , quaternion, simultaneous	1.461	0.000029	0.19756	60.195	60.195	0.77681	0.86175	0.42224	2.18684
$c_1$ , Euler angles, separable	2.952	0.000019	0.15764	39.414	39.414	1.82489	1.83352	0.95477	9.52354
$c_1$ , axis angle, separable	2.907	0.000019	0.15764	39.421	39.421	1.82478	1.83336	0.95472	9.50195
$c_1$ , quaternion, separable	5.430	0.000019	0.15764	39.422	39.422	1.82477	1.83336	0.95472	9.50182
$c_2$ , Euler angles, separable	2.254	0.000019	0.15763	39.704	39.704	1.82115	1.81528	0.95271	4.28711
$c_2$ , axis angle, separable	2.395	0.000019	0.15764	39.698	39.698	1.82112	1.81525	0.95269	4.28802
$c_2$ , quaternion, separable	2.486	0.000019	0.15764	39.699	39.699	1.82113	1.81525	0.95270	4.28724
$rp_1$ , Euler angles	48.996	0.000077	0.33695	203.549	203.549	0.66747	0.74590	0.38145	0.90042
$rp_1$ , axis angle	60.106	0.000077	0.33695	203.548	203.548	0.66747	0.74590	0.38145	0.90046
$rp_1$ , quaternion	60.997	0.000077	0.33695	203.547	203.547	0.66747	0.74590	0.38145	0.90036
$rp_2$ , Euler angles	246.888	0.000610	0.97951	1588.677	1588.677	0.65152	0.72278	0.36231	0.99779
$rp_2$ , axis angle	262.795	0.000610	0.97947	1588.564	1588.565	0.65152	0.72278	0.36232	0.99940
$rp_2$ , quaternion	267.045	0.000612	0.98097	1584.753	1584.754	0.65152	0.72279	0.36168	1.01333